Zinc Oxide Nanowire Gamma-Ray Detector with High Spatiotemporal Resolution

Daniel Craig Mayo

Dissertation
Submitted to the Faculty of the
Graduate School of Vanderbilt University
in partial fulfillment of the requirements
for the degree of

DOCTOR OF PHILOSOPHY
in

Interdisciplinary Materials Science
May, 2017
Nashville, Tennessee

Approved:

Richard F. Haglund Jr., Ph.D.
Timothy P. Hanusa, Ph.D.
Richard R. Mu, Ph.D.
Robert A. Reed, Ph.D.
D. Greg Walker, Ph.D.

To my mom, Linda.

ACKNOWLEDGEMENTS

There are no words to express how grateful I am for all the people that have been part of my life during this journey. I could not have completed my PhD without their help, and I would first like to thank the two advisors that guided me through my graduate career.

Professor Richard Mu accepted me as an REU student during my final summer as an undergraduate. After interacting with his group and getting a chance to do actual research in a lab, I changed my graduate path from computational physics to experimental physics and never looked back. Professor Mu's group has always felt like an extended family, where the members worked hard and helped each other without question. I also learned humility in his group – celebrate the victories in the lab, but be mindful of the people and path that led to that point. I honestly can't begin to express how much I appreciate everything he has done to help me and my family over the years. He has been there through all of the ups and downs in my personal and professional life, and I am honored for the chance to continue to work with him in the future.

Professor Richard Haglund accepted me into his group at Vanderbilt after I finished my Master's at Fisk University. I struggled at the beginning while trying to balance course work with research and family, and he gave me some of the best advice I've ever received. He told me that my future was in my hands and that I would fail or succeed based on my own actions. That motivated me to work harder than I had ever worked and is something I still carry with me today. I also want to thank Professor Haglund for instilling within me a deeper appreciation for the elegance of physics, from cascade lasers to perturbation theory. His depth of knowledge and work-life balance are inspiring, and I look forward to working with him in future projects.

I am also very grateful to Professors Timothy Hanusa, Robert Reed, and Greg Walker for serving on my PhD committee and for their guidance and expertise. Their detailed questions and observations have helped me examine my research from multiple perspectives, leading to a more robust understanding. Furthermore, our discussions have yielded additional insights that add strength to the overall research.

I also thank the members of the VINSE staff for their assistance throughout my time at Vanderbilt. Professor Anthony Hmelo, Dr Ben Schmidt, and Dr Bo Choi offered technical expertise and advise that often made the difference between a successful and unsuccessful characterization. In particular, Professor Hmelo has always been extremely helpful during any equipment challenges. I am also grateful for the experimental guidance of Dr Choi. His mantra of never quitting when faced with research difficulties has become one of my core values.

Professor Akira Ueda at Fisk University has been one of my most influential mentors. He was always available to help with both research and course work, even at night and on the weekends. His dedication to the students continues to be an inspiration. I would also like to thank Professor Zhengda Pan for his help when I first started working with lasers and Sergey Avanesyan for his expertise and continued assistance with laser systems.

I would also like to offer my sincere gratitude to my research partner, Claire Marvinney. I can’t begin to express how much she has helped me through my time at Vanderbilt University. After both the birth of my son and my hip-replacement surgeries, she kept the research moving forward and helped me ease back into my classes and the laboratory. Moreover, the many conversations we had were instrumental in advancing and solidifying my understanding of the research.

I owe all of the research group members at Fisk University and Vanderbilt University thanks for their assistance throughout my graduate school years. I would like to especially thank Darlene Gunther, Jennifer Jones, Senthilraja Singaravelu, Christina McGahan, Ephraim Bililign, Jordan Hachtel, and Ryan Nolen for all their help and encouragement. I have been extremely fortunate to work with such talented and generous people.

I would not have been able to make it through my PhD without the support of my family. My wife, Nicole, has been a constant source of strength and encouragement throughout my graduate career. She has always helped me persevere, even when life was extremely difficult. She is one of the most intelligent and caring people I know and is a wonderful mother to my son, Draevyn, who is a limitless supply of happiness and wonder. My wife and son are the primary sources of my motivation and joy, and I am deeply thankful for them both.

My brother, Anthony, has been one of the most profound influences in my academic and personal life. He and I took the same physics and mathematics classes throughout our undergraduate and Master's programs, worked together in Professor Mu's group, and faced the same research challenges for years. He is one of the most selfless and kind people I have ever met, and I couldn't have made it through my PhD without his help.

My mom and dad worked extremely hard to provide a solid foundation for me and my brother. I couldn't ask for better parents. My dad worked to provide for our family, and my mom put her career on hold to stay home with me and my brother. They encouraged us to reach for the stars and to always choose the right path, even if it was the more difficult one. I am who I am today due in large part to the sacrifices, encouragement, and love that my parents provided.

This dissertation is a result of work funded by the Office of Science, U.S. Department of Energy (DE-FG02-01ER45916), the U.S. Department of Defense (W911NF-11-1-0156), and from the National Science Foundation NSF-CREST Center of the Physics and Chemistry of Materials (HRD-0420516).

TABLE OF CONTENTS

Page

Appendix

LIST OF TABLES

LIST OF FIGURES

CHAPTER 1

INTRODUCTION

1.1 Motivation

Advances in medical-imaging technologies continue to improve diagnostic accuracy and increase treatment options for patients. Anatomical imaging of the physical structures within the human body has now reached unparalleled precision with submillimeter spatial resolution for both magnetic resonance imaging (MRI)[1] and computerized tomography (CT)[2]. However, the highest spatial resolution currently possible for visualizing metabolic processes is approximately 3 cm with positron emission tomography (PET)[3]. Furthermore, PET scans are much blurrier and exhibit more poorly defined boundaries than conventional imaging systems[4], and if combined with the lack of clearly defined anatomical landmarks, the clinical usefulness of PET scans can be greatly reduced[5]. This is especially important since regions of high metabolic activity can correspond to the sites of tumor growth and can provide early identification of metastases.

To address these shortcomings, PET systems have been combined with CT and MRI systems to provide composite images that combine high-structural resolution with metabolic information. Computerized tomography scans consist of multiple X-rays taken at different angles to produce cross-sectional images of the skeletal structure that are then digitally processed into a three-dimensional image. Moreover, radiocontrast agents may be administered to enhance the contrast of soft tissues such as blood vessels or the colon. Magnetic resonance imaging provides three-dimensional mapping of fatty tissue and water within a patient by detecting the presence of hydrogen using strong external magnetic fields. Functional MRIs (fMRI) provide additional imaging capabilities by differentiating blood oxygenation levels within soft tissue. In both magnetic resonance imaging systems, additional contrast agents may be administered to improve image quality.

For over two decades, PET-CT systems have been used in clinical settings, while PET-MRI systems have only recently emerged after developing PET detectors that are compatible with the high magnetic fields of MRI systems[6]. Yet even though these hybrid scanning systems can provide complementary anatomical and metabolic data, CT and MRI scans remain limited in their diagnostic usefulness in many cases, including the imaging of brain tumors and neurological abnormalities.

It can be difficult for contrast agents to pass the blood-brain barrier, resulting in lower contrast images[6]. Furthermore, CT scans are typically unable to accurately image areas near the base of the skull due to the frequent presence of image artifacts[7]. Magnetic resonance images yield more detailed information about the brain tissue than CT scans since they are generated by detecting blood flow, but they remain unable to differentiate radiation damage from tumor growth, which greatly limits their usefulness in determining the post-treatment recurrence of tumors[8].

Because of these factors, PET scans have become the primary method used specifically to both identify and categorize new and recurrent brain tumors as well as many other types of tumors[9-16]. The metabolic intensities within a PET scan image are used to grade the malignancy of a tumor, determine a course of treatment, and gauge the efficacy of treatments. However, the poorly defined spatial boundaries greatly limit its usefulness. A well-defined image could serve as a guide for excision, especially in environments where the tumor tissue is visually indistinguishable from healthy tissue. In addition, clear metabolic boundaries would provide useful information about the potential spread of tumor sites into surrounding tissue.

The primary reason for current blurry PET images is the slow response time of conventional scintillation detectors currently used in PET-scan systems[3]. The research described in this dissertation is focused on developing a new concept for gamma-ray scintillators with a much faster response time to address this problem.

Conventional PET scan scintillation detectors are typically single crystals of heavy-metal oxides or halides doped with rare-earth ions that emit ultraviolet to visible (UV-vis) photons when exposed to ionizing radiation. The scintillator crystals completely attenuate incident gamma rays due to relatively large material densities and constituent atomic numbers combined with sample volumes on the order of cm^3, as shown in Table 1. After the gamma rays are absorbed, the subsequent UV-vis emission is omnidirectional with only a small fraction of the total emission detected. Moreover, typical response times from initial high-energy excitation to UV-vis emission, given in Table 1, are of order 0.01-10 μs[17]. The state-of-the-art PET scan scintillator crystal currently used is cerium-doped lutetium yttrium orthosilicate, or LYSO, that has a response time around 40 ns and a time resolution (uncertainty) in the hundreds of ps. Other commonly used scintillators compared in Table 1 include cerium-doped lutetium orthosilicate (LSO), mixed lutetium silicate (MLS), cerium-doped gadolinium orthosilicate (GSO), cerium- and zirconium-doped gadolinium orthosilicates (GSO: Ce, Zr), cerium-doped lutetium gadolinium orthosilicates (LGSO), cerium-doped lanthanum chloride ($LaCl_3$), cerium-doped lanthanum bromide ($LaBr_3$), cerium-doped bismuth germanate (BGO), and cadmium tungstate (CWO).

Vertically oriented zinc oxide (ZnO) arrays grown by a modified vapor-solid method provide a unique workbench to address this problem with a time response orders of magnitude faster than LYSO scintillators. The nanowires are single crystals of high quality, with a

Table 1: List of scintillator crystals typically used in PET systems.

	LSO	**LYSO**	**MLS**	**GSO**	**GSO: Ce,Zr**	**LGSO**	**$LaCl_3$**	**$LaBr_3$**	**BGO**	**CWO**
Light Output *(ph/MeV)*	31000	32000	76% of LSO	7600	120% of LSO	76% of LSO	49000	65000	8500	27300
Peak Emission *(nm)*	420	420	420	430	1430	425	335	360	480	475
Decay Time *(ns)*	40-47	41	36-39	30-60	50	36-41, 65	25	15	300	14.5 μs
Density *(g/cm^3)*	7.4	7.1	7.3	6.71	6.7	6.5	3.86	5.29	7.13	7.9
Size *(mm)*	10x10x5	10x10x5	10x10x5	10x10x5	10x10x5	20x6x4	10x10x5	10x10x5	10x10x5	10x10x3

photoluminescence (PL) yield from band-edge exciton emission in the ultraviolet that is typically one hundred times larger than the PL yield from defect centers in the visible emission. By carefully engineering the local environment of the ZnO nanowires through a combination of optical-cavity effects and plasmon-exciton coupling, we show that the already highly efficient band-edge emission can be further enhanced. Moreover, the nanowires, as we shall show, permit a huge increase in overall optical efficiency because the light-emitting events that take place in the nanowire are all forward directed.

The efficiency of the band-edge emission of the ZnO nanowires has the potential to offset the scintillation material challenges of both a low interaction volume and gamma-ray stopping power. The nanowires also act as waveguides, directing the UV emission toward the detector. This process occurs on a timescale in the tens of picoseconds due to the direct bandgap of ZnO, making the nanowires ideal candidates for improved PET scan resolution.

The initial focus of this dissertation in **Chapter 1** will consist primarily of an overview of scintillation and the properties of the state-of-the-art scintillators currently in use within PET scan imaging. The synthesis and optical-emission characterization of as-prepared ZnO nanowire arrays as well as for core-shell structures will be examined in **Chapter 2** with an emphasis on enhancing the optical emission via optical-cavity effects. **Chapter 3** will focus on enhancing the emission efficiency of core-shell nanowires through plasmonic interactions with metal nanoparticles and on directing the emission via waveguiding effects. Initial investigations into the suitability of ZnO nanowire arrays as a scintillation platform are detailed within **Chapter 4** with experiments covering gamma-ray-induced damage effects. Time-dependent and dose-dependent measurements will be presented. Photoluminescence (PL) light yields before and after irradiation will also be covered. Finally, **Chapter 5** discusses the conclusions drawn from initial experiments and outlines the next steps toward the realization of a PET scan scintillator for improved image resolution.

1.2 Scintillation Overview

1.2.1 Energy Transfer

A scintillator is a material that converts high-energy, ionizing radiation into UV-vis photons that can then be acquired by optically compatible detectors. In this research, we will be focusing exclusively on gamma-ray radiation and not on alpha- or beta-particle decay. The method by which gamma-rays interact with and transfer energy to matter can be divided according to gamma-ray energy into three processes. For energies below 100 keV, the primary energy-transfer process is the **photoelectric effect**, while **pair production** is the most likely interaction at energies greater than 1.022 MeV. Between 100 keV and 1.022 MeV, **Compton scattering** is the dominant process and is the main energy-transfer process for the scintillators used in PET scan imaging. Figure 1 shows the three processes as a function of the atomic number, Z, and the gamma ray energy[18]. It is worth noting that the photoelectric effect shows a strong quartic relation between the atomic number and the probability of a photoionization event while pair production displays a quadratic relationship between the atomic number and the probability of pair production occurring.

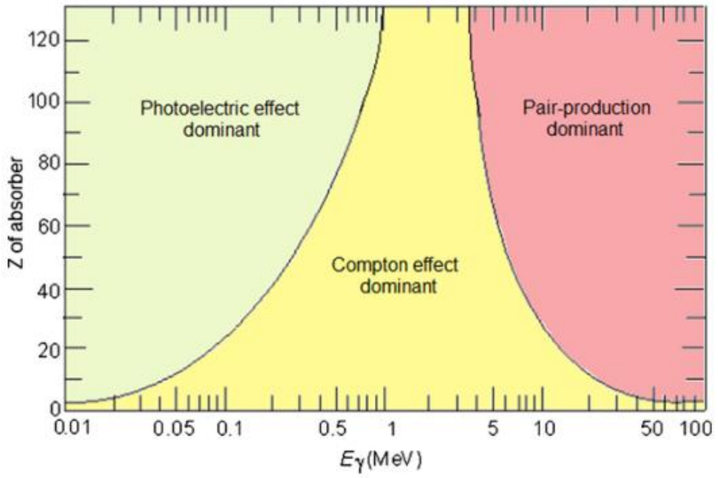

Figure 1: Three energy-transfer processes as a function of the absorber atomic number and the energy of the gamma-ray[18].

The photoelectric effect occurs when the energy of the gamma ray is completely absorbed by tightly bound, core electrons, as shown in Figure 2, resulting in the ejection of the electron followed by a potential cascade of secondary-electron absorption and ejection events. Some of the absorbed energy is used to overcome the binding energy of the electron while most is imparted to the unbound electron as kinetic energy. Core-shell holes are then filled by electrons at a higher level accompanied by the emission of an X-ray.

The probability of the photoionization event, given by τ, is strongly dependent on the gamma-ray energy and the atomic number of the atom and can be approximated by the proportionality:

$$\tau \propto \frac{Z^4}{E^3} \tag{1}$$

where Z is the atomic number and E is the energy of the gamma ray. In addition, electrons in the

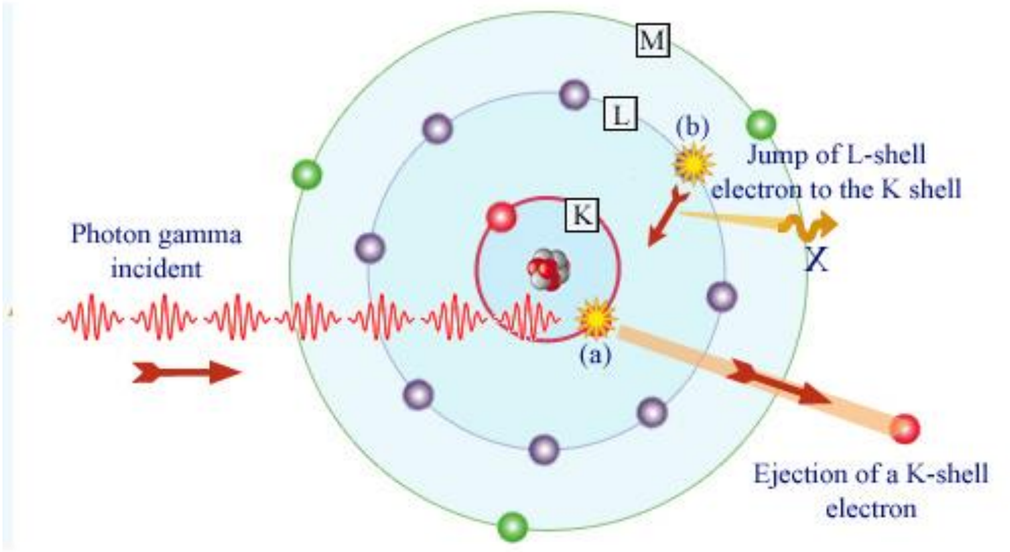

Figure 2: Schematic of the photoelectric effect. An incoming gamma ray is completely absorbed by a K-shell electron, resulting in the ejection of the electron. Following this, an L-shell electron fills the K-shell vacancy while an X-ray is simultaneously emitted. *Image courtesy of National Institute of Nuclear and Particle Physics (IN2P3)*.

K-shell are the most likely to interact with the gamma ray, accounting for up to 80% of the photoelectric absorptions[19].

Pair production occurs when a gamma ray possesses an energy of at least 1.022 MeV and passes through the electromagnetic field near an atomic nucleus as shown in Figure 3[20]. The energy is converted into an electron-positron pair, each of which requires 511 keV; any available additional energy is imparted to the pair as kinetic energy. The positron then annihilates with an electron and releases two gamma rays with 511 keV energy travelling in opposite directions. The probability of pair production increases exponentially with the energy of the gamma ray and Z^2 with the atomic number[19].

Compton scattering is the dominant energy-transfer process that occurs for gamma rays with energy between 100 keV and 1.022 MeV; the gamma ray transfers part of its energy to a

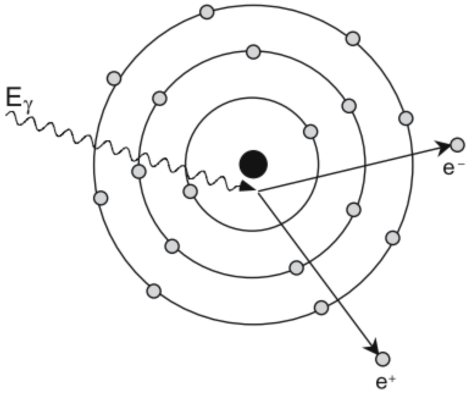

Figure 3: Schematic showing the process of pair production. When a gamma ray with energy greater than 1.022 MeV nears a nucleus, the energy may be transformed into creation of an electron and positron pair[20].

free or weakly bound, outer-shell electron. Since the binding energy of an outer-shell electron is much smaller than the gamma ray energy, the resultant kinetic energy of the scattered electron is nearly equal to the energy loss of the scattered gamma ray. The angle at which the electron and gamma ray scatter from each other depends on the amount of energy transferred and is governed by the Compton equation[20]:

$$E' = \frac{m_0c^2}{1 - \cos\theta + {m_0c^2}/{E_\gamma}} \tag{2}$$

where m_0c^2 is the rest energy of an electron (511 keV), θ is the angle between the incident and scattered gamma ray, and E' and E_γ are the scattered and incident gamma-ray energies respectively. This is depicted in Figure 4. The energy transferred is at a minimum when the scattering angle $\theta = 0°$, and at a maximum when the gamma ray is scattered back from the electron at $\theta = 180°$. Using the Compton equation, the energy of a forward-scattered gamma ray

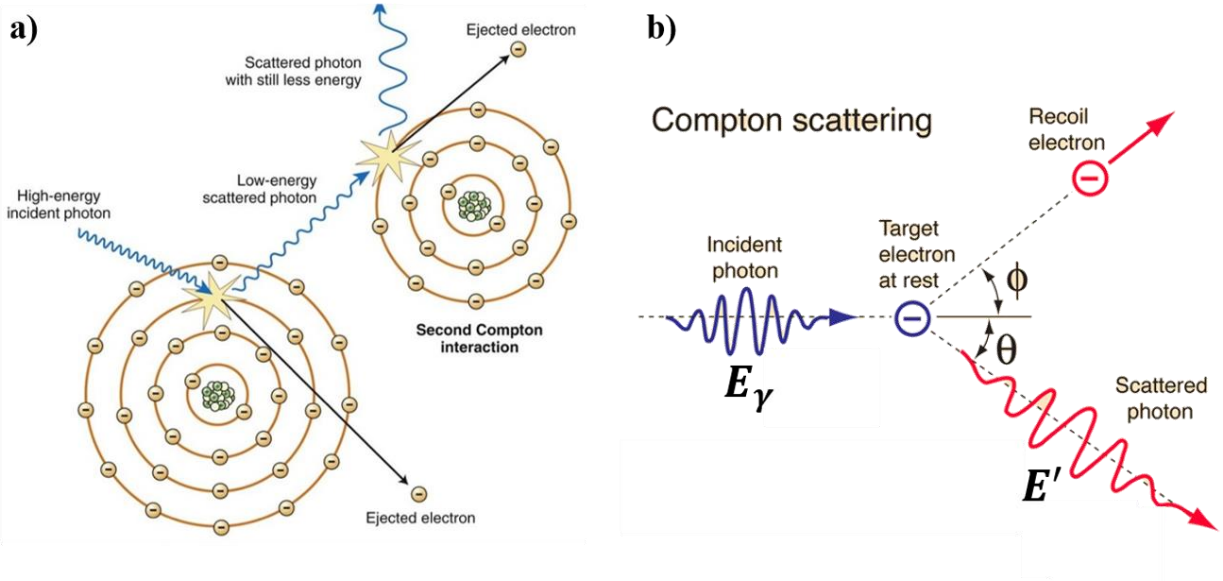

Figure 4: The Compton effect is shown in (a) wherein a high-energy gamma ray between 100 keV and 1.022 MeV is incident upon a material. Electrons within the outer shells are ionized upon colliding with the gamma ray. The energy imparted to the electron is dependent upon the Compton scattering angle shown in (b). *Image adapted from radiologykey.com and hyperphysics.phy-astr.gsu.edu.*

would be (511 keV)/1 for no change in energy while the energy of a back-scattered gamma ray would be (511 keV)/3 or approximately 170 keV.

The probability for Compton scattering is not the same for all scattering angles or energies. The probability is given by the Klein-Nishina equation[20]:

$$\frac{d\sigma}{d\Omega} = Zr_0^2\left(\frac{1}{1+\alpha(1-\cos\theta)}\right)^2\left(\frac{1+\cos^2\theta}{2}\right)\left(1+\frac{\alpha^2(1-\cos\theta)^2}{(1+\cos^2\theta)\big(1+\alpha(1-\cos\theta)\big)}\right) \qquad (3)$$

where $d\sigma/d\Omega$ is the differential scattering cross section, Z is the atomic number of the scattering material, r_0 is the electron radius, and $\alpha = {}^{E_\gamma}\!/_{m_0c^2}$. This equation is strictly true for the interaction between gamma rays and free electrons, but since electrons in the outer shell are not tightly bound, the formula is a reasonable approximation for the interactions that occur in

Compton scattering. For the initial scattering event of a 511 keV gamma ray, $\alpha = 1$, so Equation (3) reduces to approximately:

$$\frac{d\sigma}{d\Omega} = \left(\frac{1}{2 - \cos\theta}\right)^2 \left(1 + \frac{(1 - \cos\theta)^2}{(1 + \cos^2\theta)(2 - \cos\theta)}\right) \tag{4}$$

Figure 5 shows the scattered photon energy and scattering probability as a function of the scattered angle.

1.2.2 Gamma-Ray Attenuation

The attenuation of a stream of photons with the same energies and direction of travel within a material is described by Beer's law with the equation:

$$N(x) = N_0\, e^{-\mu_l x} \tag{5}$$

where μ_l is the linear attenuation coefficient, *x* is the distance travelled through the material,

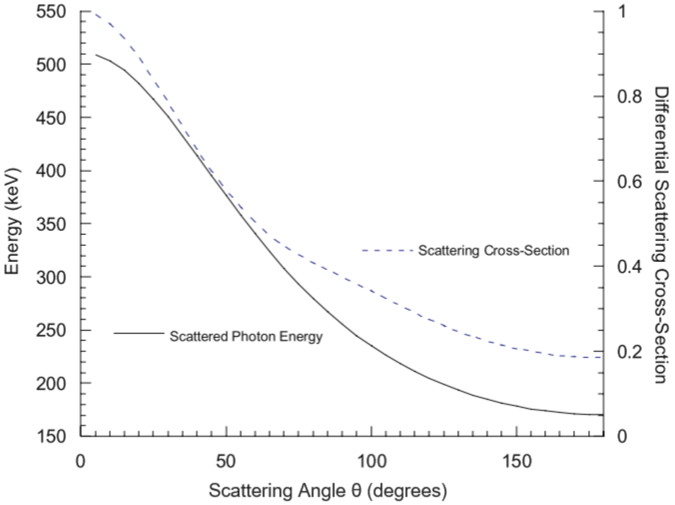

Figure 5: The Compton-scattered photon energy (left axis) and scattering probability (right axis) for a 511 keV gamma ray as a function of scattering angle[20].

N_0 is the initial number of photons, and *N(x)* represents the number of non-attenuated photons remaining at distance x. A large value of μ_l means that most of the photons will be attenuated after travelling only a short distance within the material. The reciprocal of the linear attenuation coefficient, or $\lambda = \frac{1}{\mu_l}$, is known as the mean free path.

The probability that a photon will be attenuated within a material depends on the total number of atoms in its path, not on the spatial distribution of the atoms. Therefore, it is convenient to describe this attenuation in a way that does not depend on the density of a material but is relatedto the linear attenuation coefficient. This can be achieved by defining the mass attenuation coefficient, μ_m, by:

$$\mu_l = \mu_m \times \rho \tag{6}$$

or

$$\mu_m = {}^{\mu_l}\!/_{\rho} \tag{7}$$

where ρ is the density of the material. With this convention, the mass attenuation will be exactly the same for ice, water, and steam while the linear attenuation coefficient would differ greatly. And for all materials, the attenuation coefficients are strongly dependent on photon energies with higher energies corresponding to a decrease in attenuation[18].

1.2.3 Important Scintillator Properties

Some of the most important characteristics of scintillators include:

Scintillation efficiency: The number of photons output is proportional to the energy of the gamma ray divided by the energy of the output photons and multiplied by the quantum efficiency of both the transport and luminescence phases of the scintillation process. The current state-of-the-art LYSO scintillator has a scintillation efficiency of approximately 0.2 for 662 keV gamma rays at room temperature[21].

Light yield: The fraction of generated UV-vis photons that arrive at the photodetector within a time period called the shaping time, typically between 40 ns and 10 μs. This is always a fraction of the scintillation efficiency due to the omnidirectional nature of the emission.

Gamma ray stopping power: This is primarily gauged using an attenuation coefficient for the material that is dependent on a material's density and effective atomic number; a dense, high-Z material strongly attenuates incident gamma rays. However, for energies in which the Compton effect is the dominant energy transfer mechanism, the attenuation coefficient is independent of Z[22].

Scintillation response time: The decay time for conventional scintillators is primarily a function of electron-hole transport and luminescence time. Parity and spin-forbidden transitions for most rare earth ions have decay times of μs to ms. In the case of allowed 5d-4f transitions, the response times are tens of ns. However, the fastest transitions occur with the radiative decay of Wannier excitons in direct bandgap semiconductors with values in the sub-ns range.

Radiation resistance: The performance of conventional scintillators can degrade over time due to radiation absorption causing damage to the lattice. This is a strong concern with bulk scintillators since the defects may be trapped within the large sample volume and unable to migrate effectively.

1.2.4 Conventional Rare-Earth Doped Scintillators

Conventional rare-earth doped scintillators combine the benefits of a dense, high-Z material with high quantum-efficiency luminescence. The host material typically consists of a heavy element paired with a halide/oxide/silicate, resulting in a matrix material with a density greater than 5 g/cm^{3} [23]. The dopant ion is typically a rare-earth element with a highly efficient electronic transition that is of lower energy than the bandgap of the matrix material to allow efficient transport of emitted light. The most common rare-earth dopant currently used in modern scintillators is the Ce^{3+} ion[24]. This is due to a 5d-4f transition that is spin- and parity-allowed, resulting in a fast luminescence decay of order tens of nanoseconds. Additionally, the emission wavelength is 420-440 nm which, is near the maximum quantum efficiency range of PMTs as seen in Figure 6.

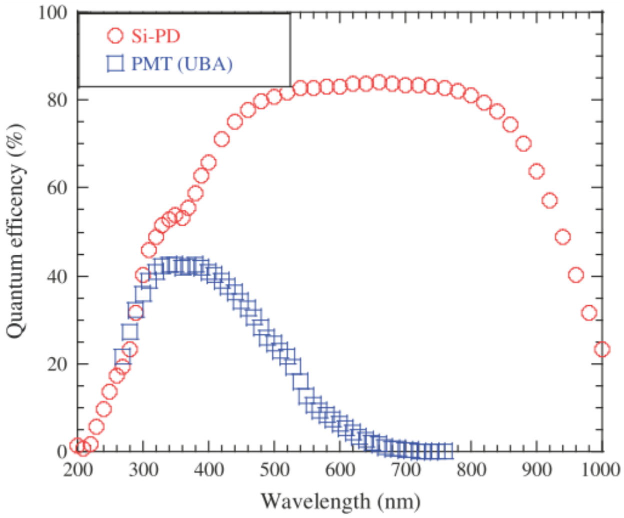

Figure 6: Quantum efficiency of a typical silicon photodetector and a PMT (ultra bialkali) as a function of wavelength[24].

For conventional rare-earth doped scintillators, the scintillation process consists of three parts: 1) energy conversion, 2) transport, and 3) luminescence[25] as shown in Figure 7. For gamma rays used in PET scan imaging, the energy-conversion process is dominated by Compton

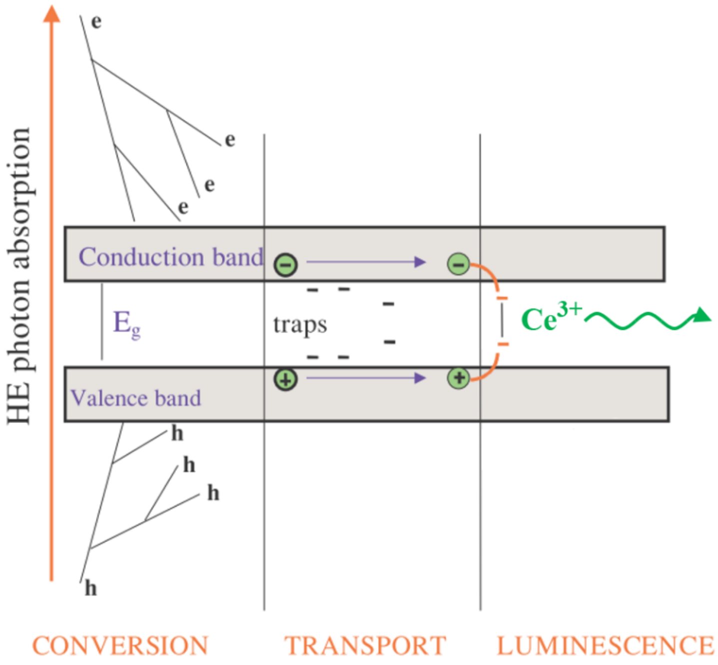

Figure 7: Scintillation process for rare-earth doped scintillators consists of conversion of ionizing radiation into electron-hole pairs, transport of the weakly bound pairs to luminescent centers, followed by transfer to the rare-earth ion and light emission[25].

scattering, in which the incident gamma ray inelastically collides with the electrons of the scintillating material. The collisions result in ionization and promotion of electrons high into the conduction band while holes are formed deep within the valence band. The electrons then rapidly thermalize to the conduction band edge, over the course of a few ps, while the holes migrate more slowly to the valence band edge.

The transport process occurs after thermalization as the electrons and holes migrate through the lattice to reach luminescent centers present in the form of doped impurity atoms. As the electrons and holes migrate, they may be repeatedly trapped into defect centers, resulting in a much slower response time for the scintillator[26]. After reaching the luminescence centers, the electron and hole recombine, yielding light in the UV-vis range. This luminescence is lower energy than that of the host-material bandgap so the emission is able to propagate through the scintillator without significant attenuation. However, since the emission is omnidirectional, only a fraction of the total emission is detected.

1.3 ZnO As a Scintillator Material

1.3.1 ZnO Properties

Zinc oxide (ZnO) is a II-VI semiconductor with a wide direct bandgap of 3.37 eV and a large exciton binding energy of 60 meV. These properties yield a band-edge exciton that is thermally stable at room temperature ($kT \approx 25$ meV), resulting in a highly efficient, near-UV emitter that has been used in a variety of applications including optoelectronics[27-29], nanolasers[30-32], and sensors[33-35].

Zinc oxide typically crystallizes into a hexagonal wurtzite structure with lattice constants of $a = b = 3.25$ Å and $c = 5.21$ Å[36]. The formation of a semi-stable zincblende structure is possible through epitaxial growth on a substrate with a cubic lattice, while a stable rocksalt structure is only achievable at pressures greater than 9 GPa[37]. The material density of ZnO is 5.61 g/cm^3, which is substantially less than that of conventional heavy-metal oxide scintillators, but is greater than that of plastic scintillators[38].

Room-temperature PL spectra for ZnO typically comprise two emission bands, as shown in Figure 8. One is a sharply defined band-edge peak centered at 3.3 eV that is due to free exciton recombination, while the other is a broad visible emission peak centered at 2.3 eV that is a superposition of various intrinsic defect emissions[39]. Furthermore, recent studies of ZnO nanorods have yielded strong evidence that the visible emissions located at 2.5 and 2.2 eV can be attributed to singly-charged oxygen vacancies (V_{O+}) and doubly-charged oxygen vacancies (V_{O++}) respectively[40].

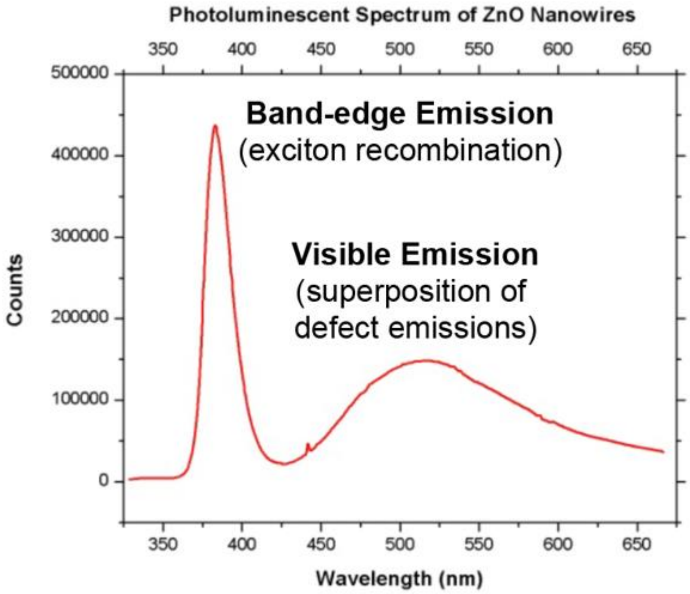

Figure 8: Typical photoluminescence spectrum of ZnO. The sharply-defined band-edge emission is due to exciton recombination and is centered around 3.3 eV. The visible emission is a superposition of defect emissions typically centered at 2.3 eV.

There has been a steady increase in research focusing on ZnO as a scintillating material over the last decade[41-51]. Some of the properties of ZnO that are appealing for scintillation applications include: high quantum efficiency light output[52], sub-nanosecond response times[53], and higher radiation hardness than other semiconductor materials such as Si, GaAs, or GaN[54].

1.3.2 ZnO Thin Film Scintillators

Approximately 50 years ago, ZnO was among the very first direct band gap semiconductors to be studied for scintillation applications. In 1966, ZnO was doped with gallium to examine the potential improvement in response time[55]. This resulted in the replacement of Zn atoms with Ga atoms and introduced a degenerate donor band overlapping the bottom of the conduction band. The electrons from the donor band recombined with the holes within the valence band with a time response faster than 1 ns, which was the limit of temporal resolution for the experimental measurement at that time. Additional experiments on undoped ZnO have found similar response times with an overall consensus that the radiative lifetime of the free exciton is highly dependent on the material quality[56].

In the case of highly-crystalline ZnO, non-radiative decay through defect channels is minimized, while the band-edge emission is extremely efficient with a yield of approximately one photon for the absorbed energy necessary to generate an electron-hole pair[57]. This is in contrast to rare-earth doped scintillators which require absorption of 2-7 times the band-gap energy to yield a photon[58], primarily due to inefficient electron-hole transport to luminescent centers within the host material[59].

1.4 Overview of Scintillation in PET Scans

One of the most promising applications for ZnO nanowire scintillators is for use as a PET scan radiation detector. A PET scan is a medical-imaging system that is used to observe biological processes and search for potential tumor and metastases sites. Tumor sites generally have a large metabolic energy demand, leading to a preferential uptake of glucose compared to normal tissue. Scans utilize this pathway by having the patient ingest a radioactive glucose analog that concentrates in tissues with increased metabolic rates.

The most commonly used radioactive glucose analog is [^{18}F-2-fluoro-2-deoxyglucose], or FDG[3]. This compound contains the radioactive isotope fluorine-18 that has a half-life of 110 minutes. As fluorine-18 decays to a stable isotope of oxygen, O-18, it emits positrons that quickly annihilate with localized electrons. The distance the positron travels before annihilation depends on the type of tissue it is generated within; water serves as a good approximation for most tissue. The mean distance a positron will travel in water before annihilation is 0.6 mm[60], so the signal generated is highly localized to the site of the positron emission. The annihilation event yields two 511 keV gamma rays that are emitted at nearly 180˚ opposite each other as shown in Figure 9.

Figure 9 also shows that the patient is surrounded by a 360˚ ring of scintillators and detectors during the scanning process. The scintillator crystals convert the gamma rays into visible light that is emitted omnidirectionally. Only the light that is incident on the detectors is counted as an event. If two such events occur 180˚ opposite each other and across the patient,

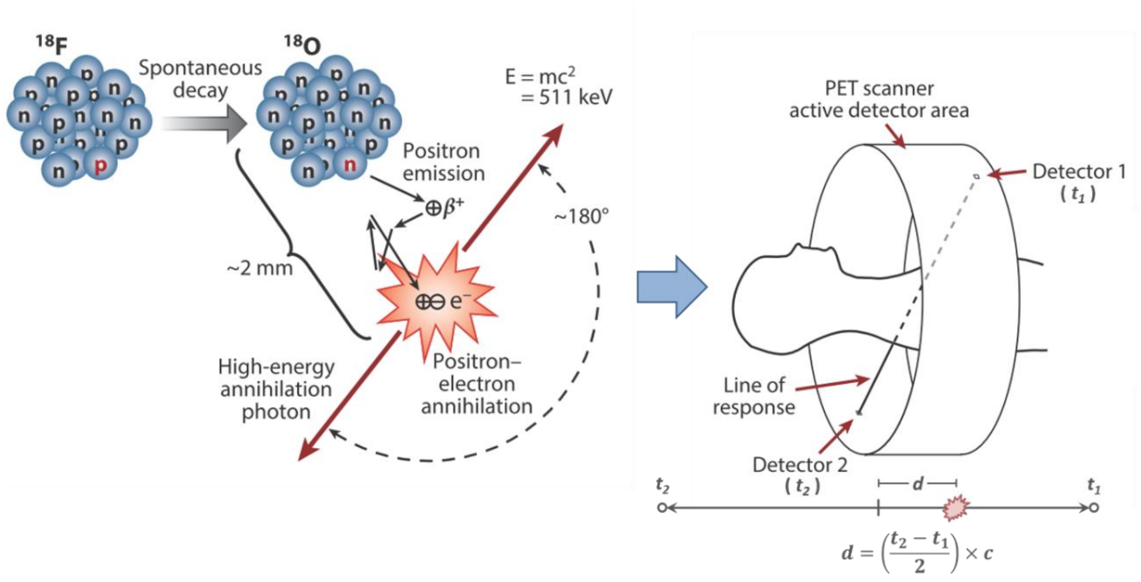

Figure 9: Overview of PET scan procedure. After a radioactive glucose analog is ingested by a patient, it is preferentially taken up by regions of high metabolic demand. As the fluorine-18 decays into a stable oxygen-18 atom, it emits a positron that annihilates with a localized electron, generating two 511 keV gamma rays 180 degrees apart. The detectors then localize the annihilation event along the line of response based on the difference in timing between the two gamma-ray detections[3].

the coincidence processing unit will calculate where along the line of response (LoR) the annihilation occurred based on the difference in the timing of the events. The distance of the event from the center of the LoR is calculated as the difference in time between the first detection, t_1, and the second detection, t_2, divided by two and multiplied by the speed of light, c.

It is also important to note that the majority of the annihilation events do not get counted by the coincidence processing unit – or are counted with erroneous LoRs. Figure 10 shows the different types of errors that can occur. No event will be recorded if the gamma rays do not travel along the plane of the detectors, or if one gamma ray is incident on a detector while the second gamma ray is out of plane. Moreover, if two such events occur, the coincidence processing unit can incorrectly assign an LoR between the two incident gamma-ray events. It is also possible to assign an LoR between two detections that occur after a Compton scattering event has changed the course of one or both of the gamma rays.

However, the largest source of error is from the uncertainty due to the inherent time resolution of the scintillator. Since the state-of-the-art scintillators currently used for PET scans

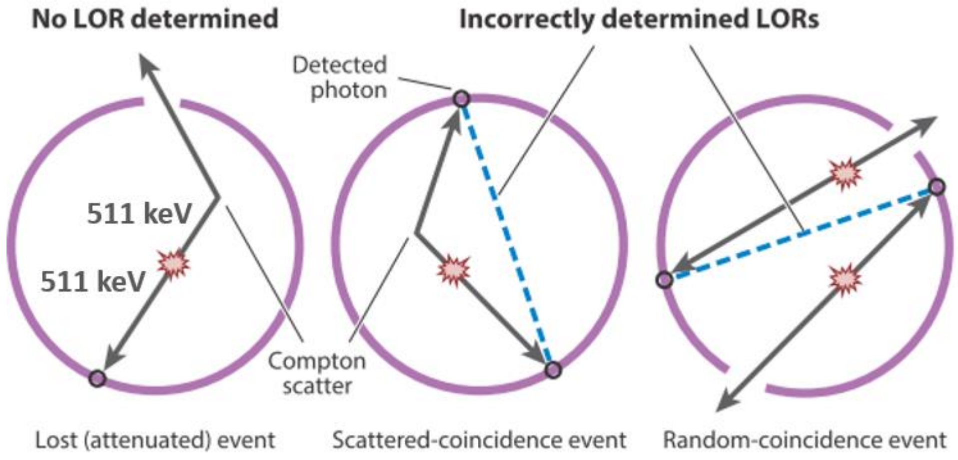

Figure 10: Possible sources of error for determining the location in space where an annihilation event occurred[3].

have a response time of 40 ns ± 200 ps, the 200 ps temporal uncertainty translates into approximately a 3 cm spatial uncertainty. This spatial uncertainty is responsible for poorly defined boundaries in PET scans, especially compared to other scan methods such as an MRI as shown in Figure 11.

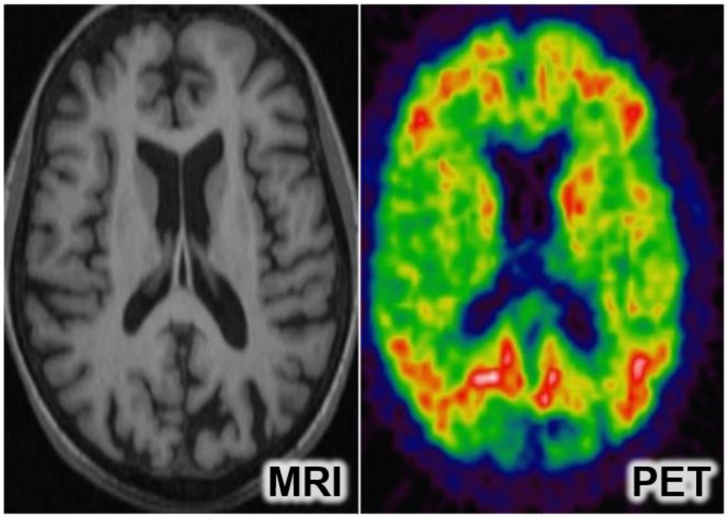

Figure 11: MRI and PET scans taken at the same location. The MRI image shows physical features with clear margins (resolution ~ 1 mm) while the PET scan shows areas of high metabolic activity with diffuse margins (resolution ~ 2 cm). *Image adapted from: Dr Paul Edison, Neurology Imaging Unit, Imperial College, London.*

The clear difference in the resolution of the images illustrates the importance of developing a new type of scintillator with a much faster time resolution.

The gamma-ray flux incident upon scintillators during a PET scan can be estimated by dividing the gamma-ray emission from a typical dosage of FDG by the surface area of a sphere with a radius equal to that of the detector ring. The number of gamma rays emitted per second by a standard dose of FDG is approximately 400 million[61]. The detector ring for a typical PET scan system is 40 cm in radius[62], which yields a spherical surface area of approximately 20,000

cm^2. Dividing the number of gamma rays per second by the surface area yields a gamma-ray flux of 20,000 per cm^2, as shown in Equation 8.

$$\frac{4\times10^{8}\ \gamma\text{-rays/sec}}{4\pi\times(40\ \text{cm})^{2}} \sim 20{,}000\ \gamma\text{-rays/sec/cm}^{2} \tag{8}$$

The typical gamma-ray fluxes from less-benign sources vary greatly depending on the source. For nuclear-reactor accidents, the gamma-ray flux for ^{137}Cs emission ranges from 150 $\gamma\text{-rays/sec/cm}^2$ at Chernobyl[63] to approximately 15 $\gamma\text{-rays/sec/cm}^2$ at the recent Fukushima disaster[64]. For nuclear warheads, the primary gamma-ray emission energy for the fissile material is 1.001 MeV. At a distance equal to the surface of the warhead, the gamma-ray flux is approximately 12.5 $\gamma\text{-rays/sec/cm}^2$ for weapon-grade uranium and 7.5 $\gamma\text{-rays/sec/cm}^2$ for weapon-grade plutonium[65]. This is for a warhead using depleted uranium for the tamper layer that is used to contain and focus the chain reaction. Conversely, if the warhead uses tungsten for the tamper layer, the gamma-ray flux drops to under 0.1 $\gamma\text{-rays/sec/cm}^2$. These values are summarized in Table 2.

Table 2: Typical gamma-ray fluxes for a variety of sources.

	Gamma-Ray Energy	**Gamma-Ray Flux ($\gamma\text{-rays/sec/cm}^2$)**
PET Scan	511 keV	20,000
Chernobyl Disaster	662 keV	150
Fukushima Disaster	662 keV	15
Uranium Warhead	1.001 MeV	12.5
Plutonium Warhead	1.001 MeV	7.5

Much of the signal from conventional scintillators is not registered by the detectors due to the omnidirectional nature of the emission. Figure 12 shows a typical scintillator/detector block setup. An 8x8 array of scintillation crystals is mounted in front of a 2x2 array of photomultiplier tubes (PMTs). In between the scintillator crystals, thin barriers of tungsten or lead, called septa, may be positioned. The septa will absorb most of the light that impinges upon their surface, collimating the emission at the expense of absorbing a large percentage of emitted photons[6].

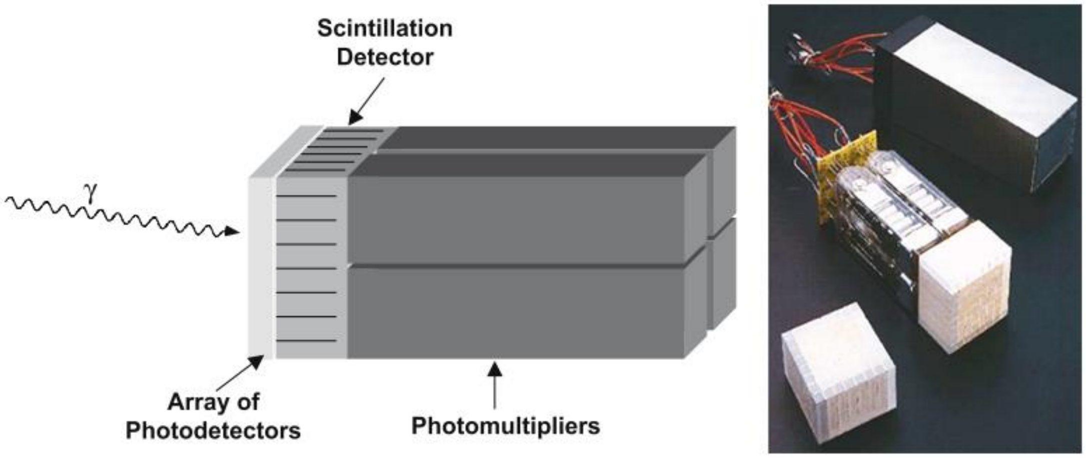

Figure 12: Diagram of a typical block detector used in PET scan systems. An 8x8 array of scintillator crystals is mounted in front of a 2x2 array of photomultiplier tubes[20].

CHAPTER 2

ZNO NANOWIRES: HIGHLY EFFICIENT EMITTERS

2.1 ZnO Nanowires

2.1.1 ZnO Nanowire Synthesis

Zinc oxide nanowire (NW) synthesis follows a protocol developed over several years with a goal of fabricating nanowires with an extremely high ratio of band-edge emission to visible emission in order to start with a system that is an efficient emitter prior to any modifications; the protocol follows. Sample substrates consisted of 500 μm thick fused-silica wafers cut to dimensions of approximately 1 cm x 2 cm with a diamond saw. These substrates were then cleaned through ultrasonication with acetone, methanol, and deionized water for 10 minutes each; compressed zero-grade nitrogen gas was then used to dry the substrates.

A 100 nm thick ZnO seed layer was deposited onto the substrates in an electron-beam evaporation chamber (Thermionics, 150-0040). A base pressure of 3×10^{-6} Torr was reached before deposition to minimize contamination. An operating pressure of less than 3×10^{-5} Torr was maintained with a deposition rate of 0.1 Å/s to minimize oxidation of the filament and ensure a uniform coating. The 100 nm film thickness was verified by a quartz crystal microbalance in situ.

Zinc oxide nanowires were then grown onto the crystalline ZnO buffer layer using a modified vapor-solid method with a vertically oriented tube furnace (Thermolyne 21100). The vertically oriented quartz tube housing used to support the substrate and gas feed lines during deposition is depicted in Figure 13. A measured amount (6.0 mg) of Zn powder was placed into an alumina crucible, which was mounted at the bottom of the 0.9 m tall quartz tube housing. The substrate was situated seed layer face-down on two silicon shelves in the substrate holder, and a fused-silica mask was placed on top of the substrate to prevent unwanted ZnO deposition on the back side of the substrate. The substrate was positioned approximately 10 cm above the crucible. Gas feed lines for Ar and O_2, a thermocouple, and exhaust vent, were fed into the growth tube through a rubber stopper. The O_2 line and thermocouple extended to directly above the level of the substrate while the Ar line was located between the substrate and crucible.

Initially, the Ar flow rate was set to 1000 sccm and the O_2 at a flow rate of 23 sccm. The higher Ar flow rate allowed the Ar gas to purge the system of ambient air and prevented the O_2 from reaching the surface of the substrate. After purging for ten minutes, the quartz tube was transferred to the vertical furnace, which was preheated to 690 °C. At this temperature the Zn source began to evaporate to the level of the substrate after five minutes, as confirmed by the appearance of zinc metal at the substrate. The Ar flow rate was then lowered to 350 sccm, allowing a partial pressure of approximately 6% O_2 to reach below the level of the substrate, and for reactions between the Zn and O_2 to occur. Zinc oxide then began to deposit onto the substrate, preferentially nucleating at grain boundaries on the ZnO seed layer. The continued growth from those locations formed the ZnO NWs. After exhausting the Zn source, the quartz tube was removed from the furnace and the sample was allowed to cool at ambient conditions.

2.1.2 ZnO Nanowire Characterization

The nanowires were then imaged by a scanning electron microscope (SEM) using a Hitachi S-4200 system with images taken in both plan view and 45˚ tilt configurations at

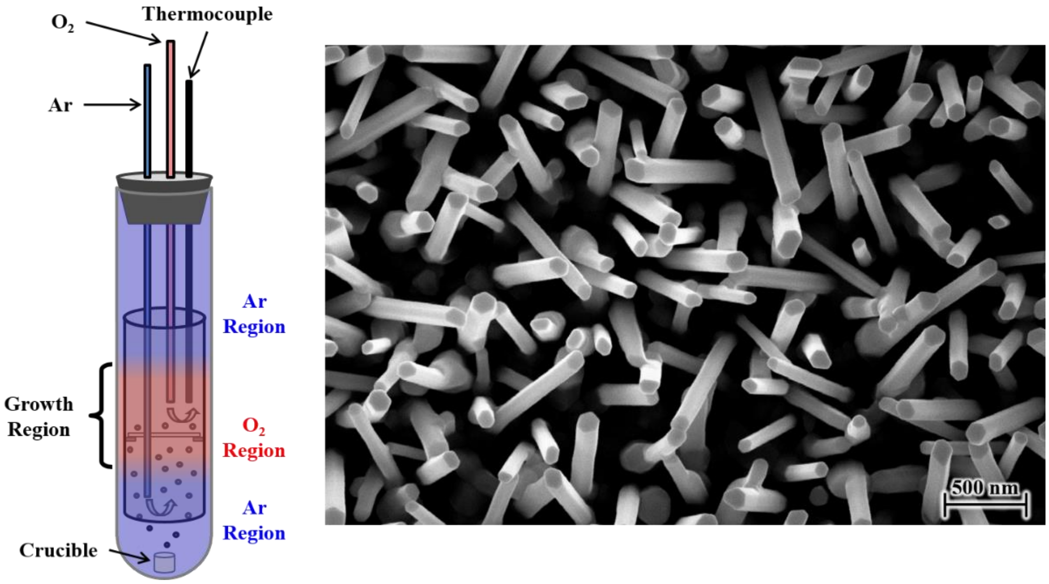

Figure 13: The vertically oriented quartz growth chamber is shown on the left with an SEM image of a typical nanowire sample on the right. For nanowire growth, the substrate is mounted face down approximately 10 cm above the crucible containing the Zn powder. The Ar gas line extends below the level of the substrate while the O_2 line ends just above the substrate.

multiple locations to verify the uniformity of nanowire morphology across the sample. Figure 13 shows a representative high-resolution image, acquired in a Raith e-Line SEM, of nanowires that are uniform in thickness, well-aligned, and have hexagonal facets at the ends; these features are typically indicative of high quality nanowires.

The SEM images were analyzed to determine an average NW height and interwire spacing of 800 nm and 400 nm respectively. The next step in fabrication was the preparation of the MgO shell layer by glancing-angle deposition as shown schematically in Figure 14. From the measurements of average NW height and spacing, the optimal rotation angle was calculated using the inverse tangent of the interwire distance divided by NW height, $\alpha = \tan^{-1}(1/2) = 27^{\circ}$. By rotating at this angle, shadowing effects between the nanowires were minimized while the uniformity of deposition along the sides of the nanowires was maximized.

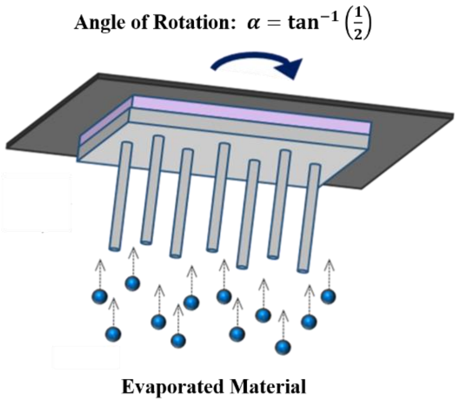

Figure 14: Schematic showing the glancing-angle deposition method used to deposit thin films or nanoparticles uniformly along nanowire samples. The optimal angle of rotation is calculated based on the average interwire distance and nanowire height.

2.2 Core-Shell Nanowires

2.2.1 Core-Shell Fabrication

The nanowire sample was then masked into octants in order to provide eight sample locations on the same substrate for subsequent experiments. The substrate was then mounted onto a glancing-angle deposition (GLAD) apparatus that was used to continuously rotate the substrate in an electron-beam evaporation chamber at the calculated angle, α. Magnesium oxide was chosen as the shell material to be evaporated onto the nanowires due to its wide bandgap of approximately 7.8 eV. Furthermore, MgO crystallizes in a rock-salt formation that has a low lattice mismatch with the wurtzite form of ZnO[66]. Magnesium oxide was evaporated onto the sample, in separate depositions for each octant, with thicknesses ranging from 0 nm to 70 nm in 10 nm increments. The resultant core-shell nanowire structure is shown in Figure 15 with an image of the sample taken by an FEI Tecnai Osiris high-resolution scanning transmission electron microscope (STEM). The interface between the ZnO and MgO is well ordered with few visible defects, which should reduce light scattering at the boundary and enhance the emission efficiency of the sample.

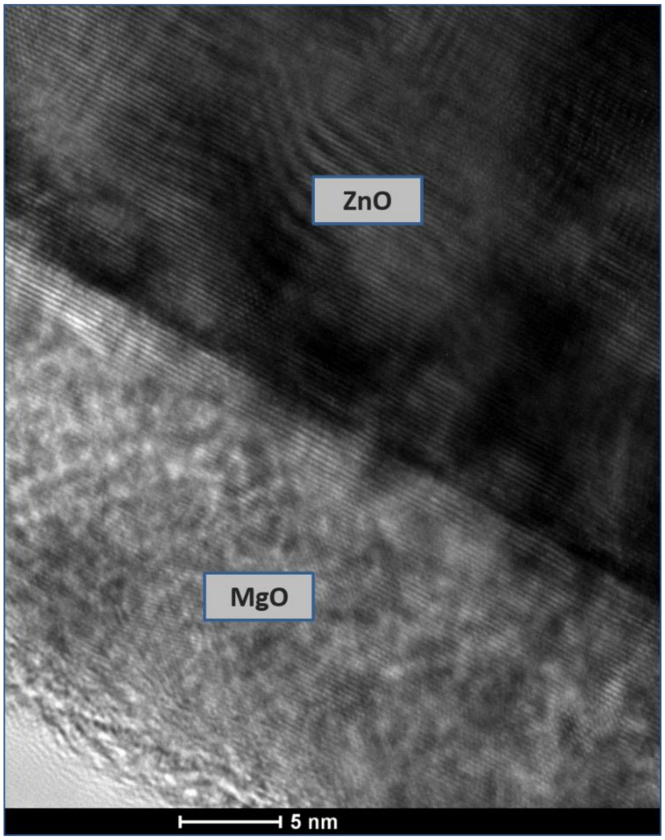

Figure 15: High-resolution TEM image of MgO coating on a ZnO nanowire. The lattice planes characteristic of a well-ordered interface show epitaxial growth of the MgO onto the ZnO, which also should reduce light scattering along the boundary.

2.2.2 Core-Shell Characterization

Photoluminescence spectra were measured with a thermoelectrically cooled (-40 °C) CCD camera in a spectroscopy set-up (HORIBA Jobin Yvon LabRAM 800HR) in the range of 1.86 eV - 3.76 eV, encompassing both the band-edge and defect emissions of the ZnO NWs. The ZnO NW emission was excited by a 325 He-Cd laser (Kimmon, 1K series 200mW vertically polarized), detected in line with the laser normal to the surface. Each measurement was the accumulation of ten measurements taken for 0.2 seconds, all with background correction. The PL spectra are shown in Figure 16.

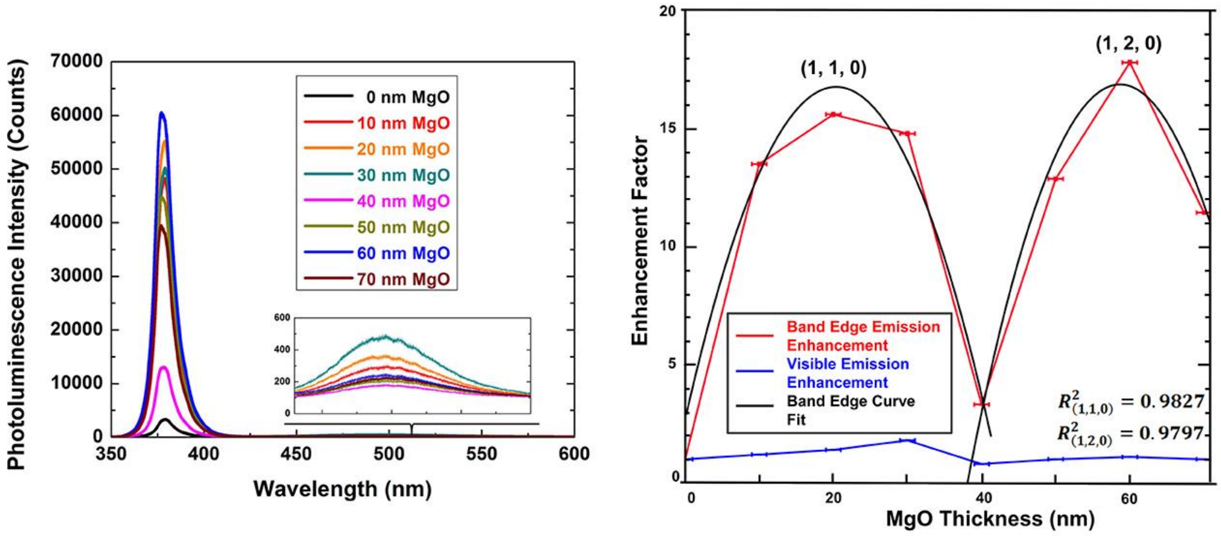

Figure 16: Left panel, photoluminescence measurements as a function of MgO coating thickness. Right panel, luminescence enhancement factor, normalized *vs* the bare ZnO nanowires. At 20 nm and 60 nm MgO thickness, there is more than a 15-fold enhancement of the luminescence compared to that of the bare ZnO nanowires.

The enhancement factors shown in the right panel of Figure 16 were calculated from the integrated areas under the emission bands in the PL spectra using a baseline and were normalized against the emission of bare ZnO nanowires. At 20 nm and 60 nm of MgO thickness, the band-edge emission is enhanced by a factor of more than 15, while the visible emission remains fairly constant. At 40 nm of MgO thickness, the emission is enhanced three-fold. This is the minimum enhancement seen and can be explained by the strong passivation effect that an MgO coating can have on the surface states on the ZnO nanowires, as reported in literature[66-71]. However, passivation effects alone cannot account for the large emission enhancement seen at 20 nm and 60 nm; the oscillatory nature of the enhancement suggests optical cavity effects.

There are two principal types of resonant modes that can be established inside a regular hexagonal cavity as in Figure 17. The first is a Fabry-Perot mode in which light is trapped between two parallel facets. The second mode is a whispering gallery mode (WGM) that occurs as light travels circularly around the interior of the cavity. For an elongated hexagonal cavity, light can still be trapped in Fabry-Perot and whispering gallery modes as shown in Figure 18, but the optical path length may differ significantly[73]. Since the as-prepared ZnO nanowires that were imaged in Figure 15 consisted of elongated hexagonal cross sections, it is likely that both modes still occur within the core-shell nanostructures. This effect can also explain some of the enhancement seen for non-resonant MgO thicknesses. Since the SEM images show that the ZnO nanowire hexagonal cross sections are dominated by the regular polygonal structure; however, there is a moderate range of cross-sectional shapes that are elongated from the regular hexagon. Thus a band of wavelengths should resonate within the optical cavities of varying cross sections,

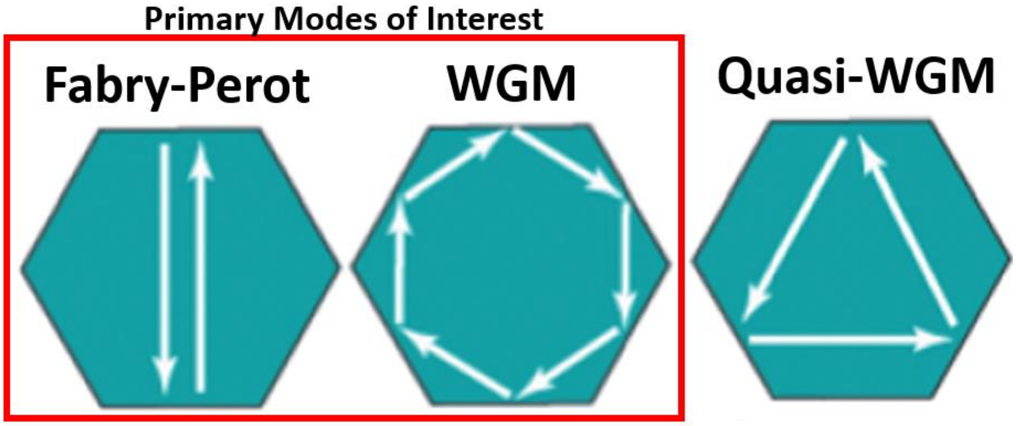

Figure 17: Resonant modes for hexagonal cavities include, from left to right: Fabry-Perot, whispering gallery mode, and quasi-whispering gallery mode. The principal modes of interest in this research are the Fabry-Perot and whispering gallery modes[72].

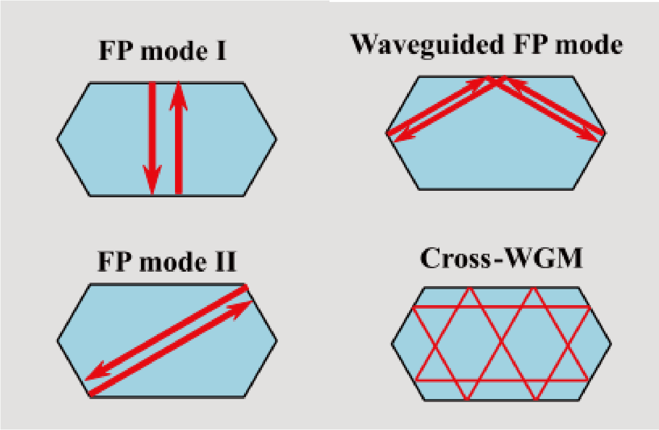

Figure 18: Optical cavity modes for elongated hexagonal cavities. Both Fabry-Perot and whispering gallery modes are still possible, albeit with altered optical path lengths[73].

leading to an overall efficiency enhancement for all MgO thicknesses. In addition, optical modes have been shown to exist for both triangular and square ZnO cavity geometries recently, which adds even more potential resonant conditions[74, 75].

Optical cavity effects have been well-documented to significantly enhance the band-edge emission of ZnO micro- and nanostructures[76-79]. This enhancement has been shown, for example, to drastically reduce the threshold for nanowire lasing, especially when exploiting the high Q factor resulting from the total-internal reflection that occurs in whispering gallery modes[32, 80]. However, even Fabry-Perot resonant modes can significantly enhance the band-edge emission and have been used for lasing applications[81].

For core-shell nanowires, the differing mode geometries are of particular importance. Fabry-Perot resonant modes set up across the diameter of the nanostructure and pass through both the core and the shell. However, in the case of whispering gallery modes, the light is trapped primarily around the interior of the shell. This has been studied using tapered ZnO microrods that are thicker in the middle of the rod than at the ends[82]. Both experimental data and finite-difference time-domain (FTDT) simulations confirm the presence of whispering gallery modes only in the thicker portions of the microrod while Fabry-Perot modes are seen throughout the length of the microrod, resulting in a hybrid mode structure when the two modes overlap.

2.2.3 Optical Cavity Modes: Calculations

The thickness of the MgO coating, *m*, that results in a resonant condition can be calculated by using straightforward standing-wave analysis with a slightly modified version of a square resonant-cavity equation[83] that properly accounts for the hexagonal shape of a ZnO nanowire of diameter $a = z + 2m$, as shown in Figure 19:

$$\frac{n_{eff}}{\lambda} = \sqrt{\frac{j^2 + k^2 + l^2}{4a^2}} \tag{9}$$

The effective refractive index, n_{eff}, of the core-shell nanowire can be written as a weighted average by the following equation:

$$n_{eff} = \frac{(z \times n_z) + (2m \times n_m)}{z + 2m} \tag{10}$$

Here, z and n_z , and m and n_m , are the thicknesses and refractive indices of the ZnO nanowire and the MgO coatings respectively. Solving for the MgO thickness, *m*, that results in a resonance condition gives:

$$m = \frac{\lambda\sqrt{j^2 + k^2 + l^2} - 2(z \times n_z)}{4n_m} \tag{11}$$

The resonant modes are given by integer values of *j, k, l* with λ as the band-edge emission wavelength of 380 nm. For ZnO nanowires of approximately 90 nm in diameter, Figure 19 shows the calculated MgO thicknesses for the (1, 1, 0) and the (1, 2, 0) modes. The calculations show resonant conditions occurring at thickness values of approximately 20 nm and 60 nm. This is in good agreement with the measured band-edge emission maxima. Additionally, the visible emission does not show any enhancement over the range of MgO thicknesses. This is also in agreement with the experimental data since no resonant modes can occur under this system using the much longer visible emission wavelengths.

2.2.4 Optical Cavity Modes: COMSOL Simulations

To provide additional insight into the enhanced band-edge emission seen at specific thicknesses of MgO, the system was simulated using COMSOL Multiphysics. Figure 20 shows the model that was developed for the simulations. Since the nanowires are much smaller than the

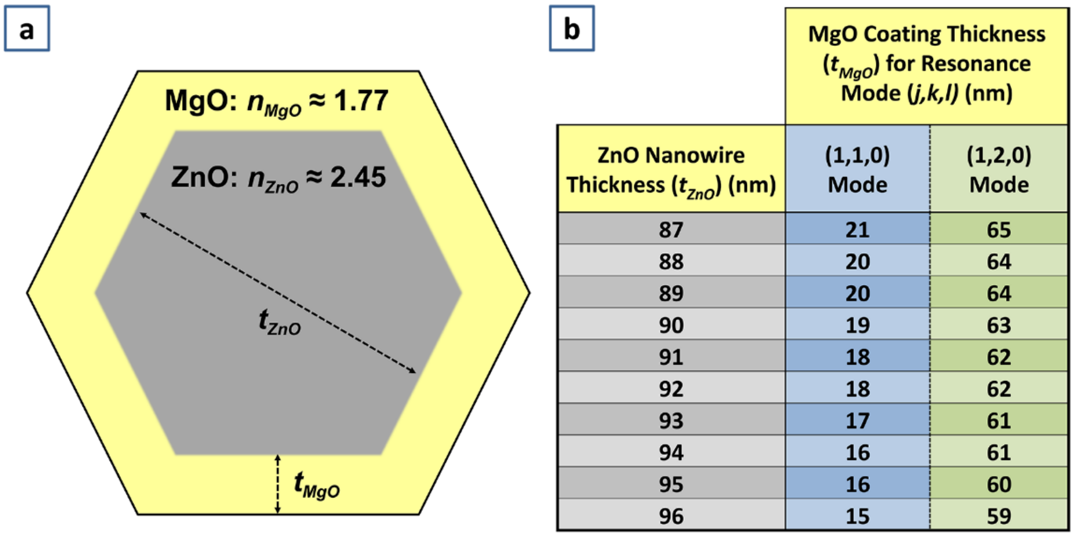

ZnO Nanowire Thickness (t_{ZnO}) (nm)	MgO Coating Thickness (t_{MgO}) for Resonance Mode (*j,k,l*) (nm)	
	(1,1,0) Mode	(1,2,0) Mode
87	21	65
88	20	64
89	20	64
90	19	63
91	18	62
92	18	62
93	17	61
94	16	61
95	16	60
96	15	59

Figure 19: Calculated MgO thicknesses that result in resonance conditions for Fabry-Perot modes. For ZnO nanowires approximately 90 nm in thickness, resonance occurs for 19 nm and 63 nm.of MgO thickness. This is in close agreement with experimental results where maximum band-edge emission intensity occurs at MgO thicknesses of 20 nm and 60 nm.

wavelengths of the simulated light sources, a plane wave was used with the propagation direction set from left to right from Boundary 3. Perfectly matched layers (PMLs) were used at the top and bottom of the model to prevent scattering at large angles while a scattering boundary condition (SBC) at Boundary 21 was used to prevent scattering at small angles.

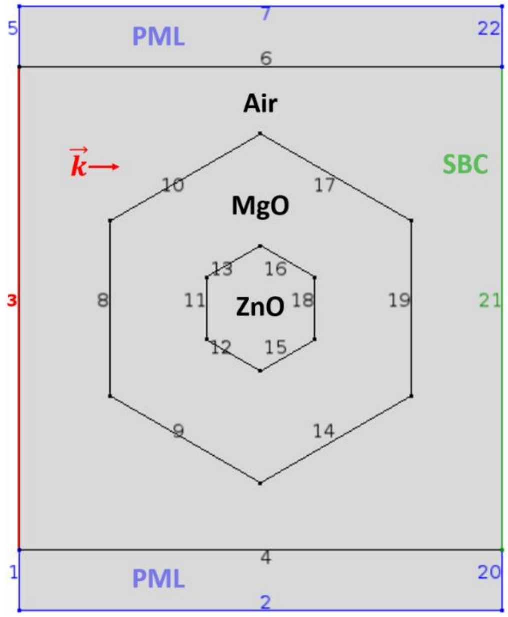

Figure 20: COMSOL Multiphysics simulation diagram for ZnO-MgO core-shell nanowire. A plane wave was used as the light source with a direction of travel from left to right from Boundary 3. Perfectly matched layers (PMLs) and a scattering boundary condition (SBC) were used to minimize reflection.

The ZnO nanowire core was held fixed at 90 nm diameter while the MgO shell varied from 0 nm thickness to 80 nm thickness in 2 nm increments. The first light source that was simulated was 325 nm; that corresponds to the wavelength used by the He-Cd laser used as the excitation source for photoluminescence measurements. The second light source that was simulated was 380 nm and corresponded to the wavelength emitted by the band-edge excitons of the ZnO nanowires. The optical constants used for ZnO at 325 nm and 380 nm were n = 2.04, k

= 0.41 and *n* = 2.48, *k* = 0.15 respectively, while the optical constants used for MgO were *n* = 1.79, *k* = 0 and *n* = 1.77, *k* = 0 respectively. The potential reflection at the interface between the oxides due to the difference in refractive indices is mitigated by the tendency of Mg^{2+} to diffuse into Zn^{2+} sites to form a graded index with $Zn_{1-x}Mg_xO$[84, 85].

After the simulations were run, the resultant steady-state electric field intensities within the core-shell nanostructures were integrated to compare the enhancements from the different MgO thicknesses. The first simulation result, shown in Figure 21, shows the optical-cavity effects from a 380 nm light source interacting with the core-shell nanowires. The highest integrated efficiencies were found at 20 nm and 60 nm of MgO thickness. This is in good agreement with both experimental data and calculations. At 20 nm of thickness, the first Fabry Perot mode sets up inside the nanostructure horizontally.

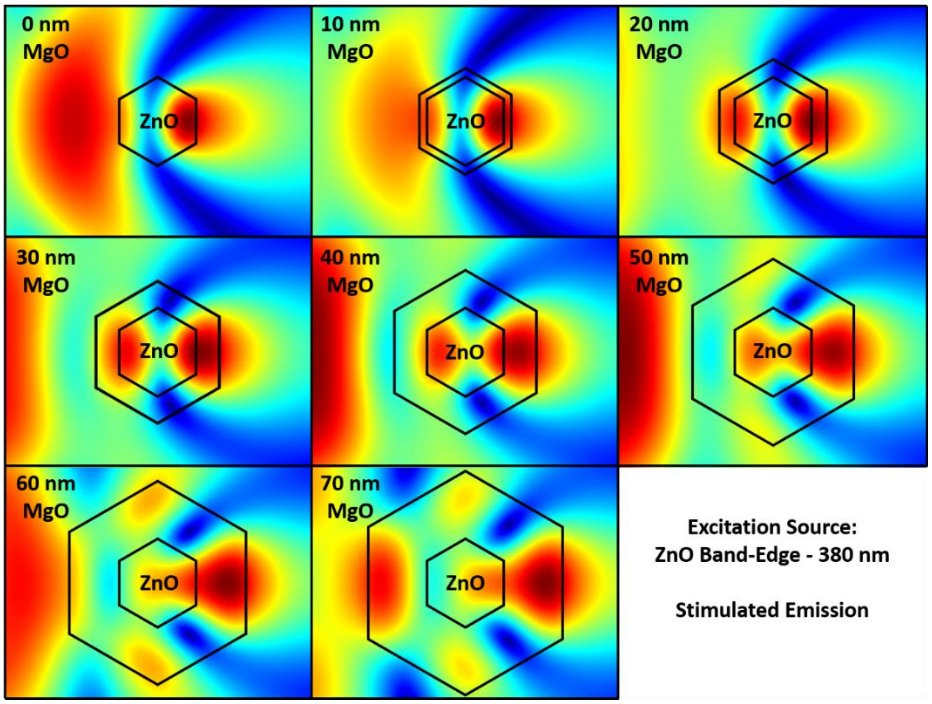

Figure 21: COMSOL Multiphysics simulations for the interaction of 380 nm light with ZnO-MgO core-shell nanostructures with varying MgO thickness from 0 nm to 70 nm in 10 nm increments; the highest integrated intensities correspond to 20 nm and 60 nm MgO thickness. Fabry-Perot modes are seen at both thicknesses with whispering gallery modes appearing at 60 nm.

The results for the 325 nm light source simulations are shown in Figure 22. The highest integrated intensities were now seen to occur at 10 nm and 50 nm of MgO thickness. This matches theoretical expectations given that the 325 nm wavelength is shorter than the 380 nm wavelength, and therefore the resonant conditions would also be expected to occur in regions with thinner MgO coatings. However, this is still close enough to the 20 nm and 60 nm intensity maxima seen for the 380 nm light source to contribute to the large enhancement that is seen experimentally.

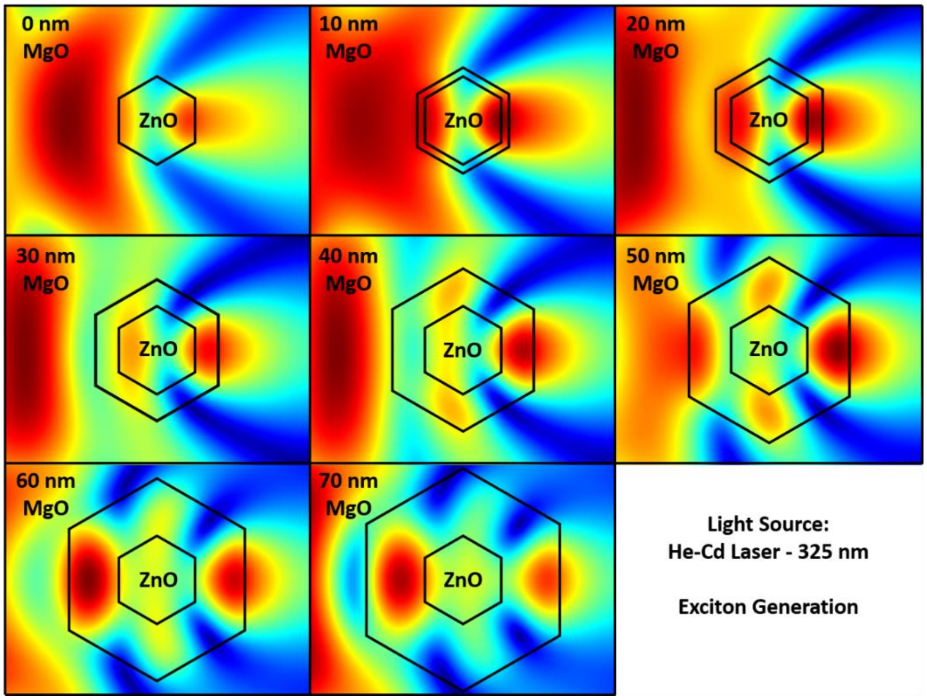

Figure 22: COMSOL Multiphysics simulations for 325 nm light interacting with ZnO-MgO core-shell nanostructures. The thickness of the MgO varies from 0 nm to 70 nm in 10 nm increments. The highest integrated intensities correspond to 20 and 50 nm of MgO, respectively. Fabry-Perot modes are seen at both thicknesses while whispering gallery modes appear at 50 nm.

The 325 nm light source generates excitons within the ZnO core. As the Fabry-Perot cavity traps the laser light, the optical path length increases as the light makes multiple passes through the ZnO. The 380 nm wavelength corresponds to band-edge emission from excitons generated in the ZnO. As the Fabry-Perot and whispering gallery modes trap the ZnO emission, that light can in turn stimulate emission from the band-edge excitons, increasing the radiative efficiency. Light trapped within the whispering gallery mode does not strongly affect the emission since it is primarily confined within the 50-60 nm MgO shell. This can explain why both the 20 nm and 60 nm of MgO coating result in approximately the same fifteen-fold emission enhancement.

CHAPTER 3

PLASMONIC EFFECTS AND WAVEGUIDING

3.1 Plasmon Interactions

3.1.1 Plasmon Overview

Plasmons are quasiparticles that arise from the collective oscillations of the free electron gas in a metal relative to fixed positive ion cores that are driven by the electric field component of incident light. Localized surface plasmons (LSPs) and localized surface-plasmon resonances (LSPRs) arise when light interacts with metal nanoparticles small enough that the oscillating electric field vector can be assumed to be roughly constant over the volume of the nanoparticle (quasi-static approximation). Coherent excitation of the plasmon field only occurs when the size of the metal nanoparticles is much smaller than the wavelength of an incident light beam. In the case of the light sources, 325 nm and 380 nm, and metal, Ag, used in this research the size of the nanoparticles is limited to tens of nanometers for an LSP response. The resonance frequency of the localized surface plasmon is strongly dependent on nanoparticle material, size, shape, and nearby dielectric environment, with the oscillations of the free electrons generating a strong localized electric field with a range of a few tens of nanometers from the metal nanoparticles.

3.1.2 Decorating Core-Shell Nanowires with Silver Nanoparticles

To study plasmonic interactions with the excitons in the core-shell ZnO-MgO nanowires, the entire sample was coated with a 10 nm nominal layer of silver using the GLAD apparatus. At this thickness, the silver coating was in the form of nano-islands on the surface of the MgO rather than a continuous film. Once the nanowires were decorated by the Ag nanoparticles, photoluminescence spectra were then acquired using the same protocol as with the core-shell nanowires. This procedure ensured that the only varied parameter was the addition of the Ag nanoparticles, as the provenance of the core-shell nanowires could not necessarily be guaranteed had they been fabricated in a second deposition cycle.

To study the morphology and uniformity of the MgO coating and Ag nanoparticles, high-resolution SEM and STEM images were taken using a Raith eLine and an FEI Tecnai Osiris respectively. Figure 23 displays high-resolution SEM and STEM images of the uniform NW coverage that resulted from depositing 10 nm of Ag using the GLAD apparatus. Graphic

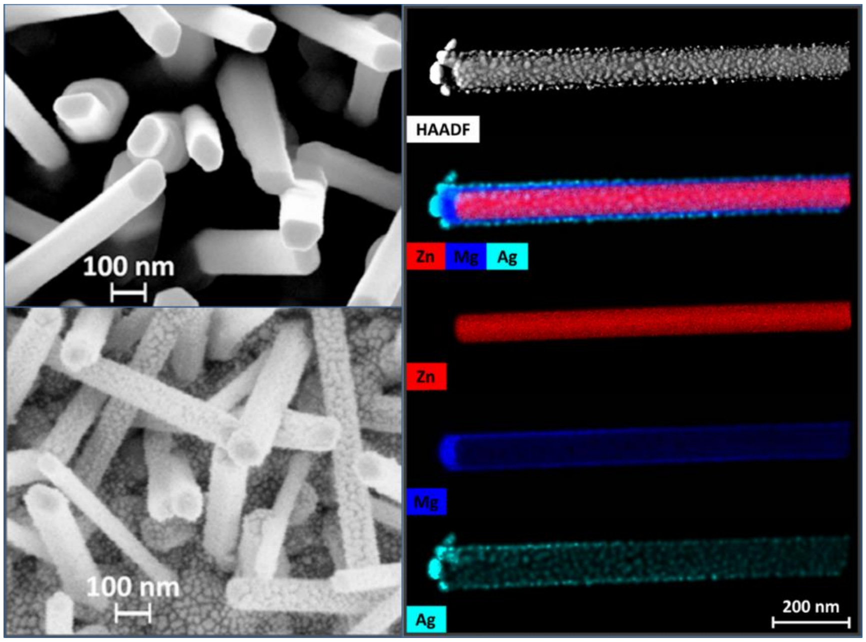

Figure 23: The upper left SEM image shows the highly faceted ZnO nanowire surfaces, while the bottom left SEM image displays the same nanowire sample after 10 nm of Ag was deposited. A high-resolution STEM image of an Ag-decorated core-shell nanowire is shown on the right. The top-right image displays the morphology of the surface of the nanowire, while the remaining images show the elemental composition.

analysis of the SEM images using *ImageJ* software found that the average size of the Ag nanoparticles was approximately 25 nm in diameter, with 70% coverage uniformly across the surface of the ZnO NWs. The deposition of magnesium, corresponding to the MgO coating, and silver was also shown in the elemental-analysis images. The MgO coating was deposited along the lengths of the ZnO nanowires, with only a slight increase in thickness at the ends of the nanowires. The MgO coating not only provided additional optical path lengths for optical cavity modes to set up within the core-shell structure, but it also allowed for distance-dependent effects on plasmonic enhancement to be studied, which was critical for interpretation of subsequent photoluminescence measurements.

3.1.3 Plasmonic Effects on Emission

Figure 24 shows the plotted emission enhancement and room-temperature PL spectra of the ZnO nanowires with varying thicknesses of MgO functionalized with Ag nanoparticles. The

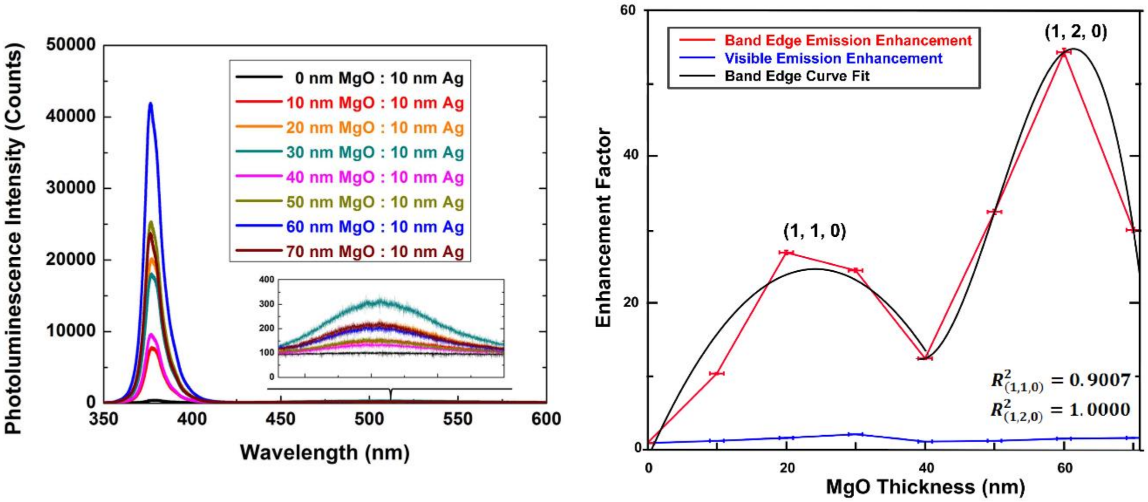

Figure 24: Left, photoluminescence spectra of Ag-decorated core-shell nanowires. The emission enhancement normalized against the bare ZnO nanowire is shown on the right. At 20 nm MgO thickness, the band-edge luminescence is enhanced approximately 25 fold while at 60 nm of MgO thickness, the emission is enhanced 55 fold.

same oscillatory enhancement to the band-edge emission that was seen in the PL measurements for the undecorated nanowires is also seen after the Ag-nanoparticle deposition. However, at 20 nm of MgO thickness, the enhancement to the band-edge emission is increased approximately 25 fold, while at 60 nm the enhancement is increased 55 fold. Also, as seen previously, the visible emission remains relatively constant, independent of the MgO thickness.

The drastic enhancement of the band-edge emission seen in the ZnO/MgO/Ag structures can be attributed primarily to plasmonic effects. The enhancement seen at 20 nm of MgO thickness can be due to the large increase in the density of states from the presence of the LSPs in the Ag nanoparticles. The transition rate is described by Fermi's Golden Rule No. 2 as:

$$\Gamma_{i \to f} = \frac{2\pi}{\hbar} |\langle f|H'|i\rangle|^2 \rho \tag{12}$$

where Γ is the transition rate of the exciton from an excited state to the ground state, $|\langle f|H'|i\rangle|$ represents the dipole matrix element that when squared yields the probability of a transition, and ρ represents the joint density of states available for the transition. The plasmons generated in the Ag nanoparticles greatly increase the local density of states which in turn increases the transition rate and results in an enhanced radiative emission and reduced non-radiative losses.

The large emission enhancement seen at 60 nm can be attributed to a different process. At 60 nm of MgO shell thickness, the electric field intensity of the LSPs from the Ag nanoparticles will be strongly attenuated and have little effect on the ZnO core. Instead, the enhancement can be explained by the light that is propagating in whispering gallery modes inside the MgO shell. As the light reflects from the exterior MgO surfaces along the hexagonal facets, it is potentially back-scattered by the plasmons into the cavity and across the ZnO core. This effectively greatly enhances the amount of light that interacts with the ZnO core and results in the 60-fold enhancement to the band-edge emission.

To provide additional insight into the enhancements, we numerically analyzed the change in band-edge emission enhancement factors over thicknesses by fitting quadratic and cubic equations to the PL yield. The first set of equations was for the MgO shell only with no Ag nanoparticles. The first equation was for the thicknesses $m \leq 40$ nm, and another for $m \geq 40$ nm, which yielded:

$$p_1(m) = -.03x^2 + 1.4x + 2.7 \tag{13}$$

$$p_2(m) = -.03x^2 + 4.7x - 120.2 \tag{14}$$

For the enhancement seen in the Ag-nanoparticle decorated core-shell nanowire, both quadratic and cubic terms were needed to fit the data. As before, the first equation was for thicknesses $m \leq 40$ nm, and the second was for $m \geq 40$ nm, which yielded:

$$p_1(m) = -.04x^2 + 2.1x - 1.2 \tag{15}$$

$$p_2(m) = -.01x^3 + 1.2x^2 - 58.6x + 903 \tag{16}$$

The root mean square deviations for these fits were 1.7, 1.5, 4.8, and 10.7, respectively.

The only fit that required a cubic equation was for the measurements that included the 60 nm of MgO thickness with Ag nanoparticles. This is due to the drastically different enhancement mechanism of the plasmons backscattering the light that is propagating in whispering gallery modes back into the ZnO core. By doing so, additional Fabry-Perot modes can be generated which in turn greatly enhances the emission of the ZnO.

3.2 Cathodoluminescence Measurements

3.2.1 Cathodoluminescence Experiment

To further characterize the Ag-decorated core-shell nanowire sample, high-angle annular dark field (HAADF) images and cathodoluminescence (CL) measurements were acquired as part of a collaboration at Oak Ridge National Laboratory. The microscope system used was a VG-HB601 aberration-corrected STEM operated below 60 kV to increase the interaction between the beam and the sample. Both high-angle annular dark field images and cathodoluminescence measurements were taken simultaneously to provide complementary morphology and emission information. Cathodoluminescence measurements use a focused beam of above-bandgap energy electrons to excite the luminescent centers within the sample. The emission can then be spatially resolved as the beam rasters across the sample. High-angle annular dark field imaging provides high-quality images of the morphology of the sample and is especially sensitive to contrasts in the atomic number of the atoms comprising the sample. Figure 25 depicts the experimental arrangement used for the measurements.

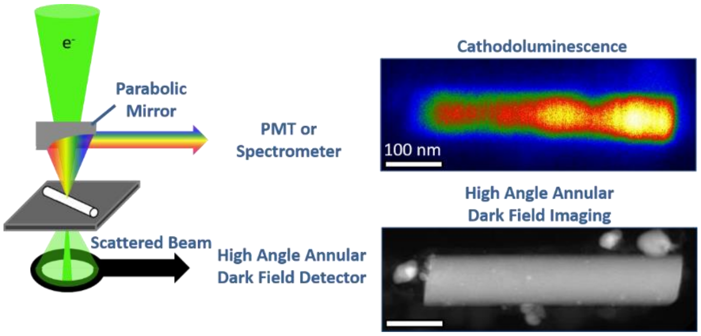

Figure 25: Schematic showing the imaging configuration for both the HAADF and CL measurements of the Ag-decorated core-shell nanowires. *Images courtesy of Jordan Hachtel.*

3.2.2 Plasmonic Effects

The HAADF and CL measurements taken of a core-shell nanowire with a non-uniform Ag-nanoparticle distribution are shown in Figure 26. The HAADF image shows that the nanowire has alternating areas of high and low Ag-nanoparticle concentration. In the areas of high nanoparticle concentration, the CL measurements show strong band-edge emission from the nanowire. Conversely, the areas that show low Ag-nanoparticle coverage display the lowest band-edge emission. This direct correspondence of the enhancement of the band-edge emission with the presence of the Ag nanoparticles verified that the ZnO band-edge emission can be strongly enhanced through plasmonic interactions, potentially leading to a greatly enhanced scintillating material.

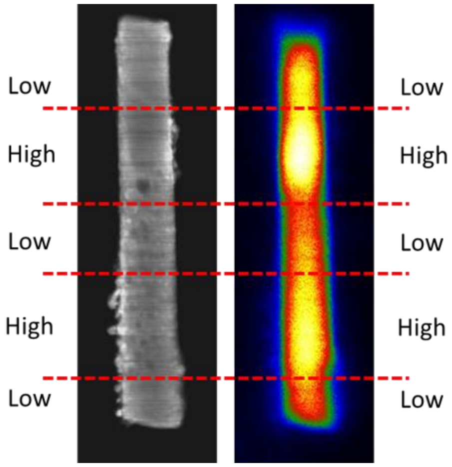

Figure 26: High-resolution HAADF (left) and CL (right) images of a ZnO-MgO core-shell nanowire non-uniformly decorated with Ag nanoparticles. The HAADF image shows the nanowire has alternating areas of high and low Ag-nanoparticle coverage. The CL measurement shows that the areas with the higher concentration of Ag nanoparticles correspond to the most intense emission.

3.2.3 Waveguiding Effects

Waveguiding effects also have the potential to greatly enhance the efficiency of a ZnO nanowire scintillator. By channeling the band-edge emission along the length of the nanowire, virtually all of the emitted light will reach the detector. This is in contrast to the omnidirectional emission of typical scintillators that results in the majority of the emitted light not being detected, as seen in Figure 27.

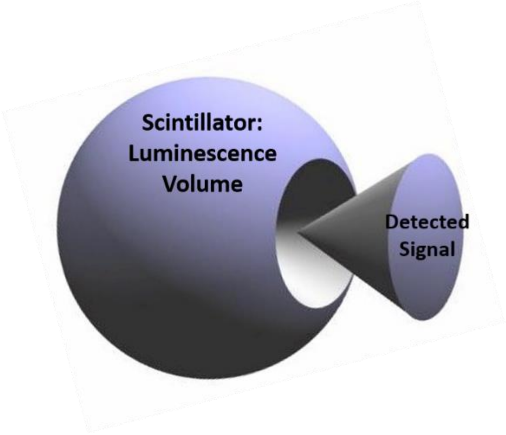

Figure 27: Conventional omnidirectional scintillator emission results in a small fraction of the signal being detected.

ZnO nanowires with their hexagonal structure and sharp faceted ends provide an ideal morphology for waveguiding and have been researched extensively for this property[86-89]. The wavelength of the light, cavity diameter, and coupling angle can all strongly affect which optical modes set up inside of the nanowire cavity and whether efficient waveguiding will occur. For the band-edge emission at approximately 380 nm, the fundamental, Fabry-Perot mode is the most efficient and tends to be the dominant mode for ZnO nanowires with diameters between 90 and 150 nm[90, 91]. Photoluminescence measurements of waveguiding efficiency of the band-edge emission in ZnO nanowires has shown that these single modes are capable of confining 80-90%

of the light[92, 93]. In addition, cathodoluminescence experiments have clearly shown that ZnO nanowires exhibit strong waveguiding behavior[94, 95].

To experimentally verify waveguiding within an Ag nanoparticle-decorated, core-shell ZnO nanowire, additional cathodoluminescence measurements were performed at Oak Ridge National Laboratory. Figure 28 shows the results of that experiment. The top image is a high-resolution TEM image of a core-shell ZnO-MgO nanowire that is uniformly decorated with Ag nanoparticles. The uniformity of the nanoparticles is important to avoid any intensity hotspots due to plasmon interactions. The bottom image shows cathodoluminescence measurements of the same nanowire. The highest intensities are seen at the ends of the nanowire with the most intensity occurring at the end that was broken off the sample and is not covered with Ag nanoparticles; here, the confined light is able to escape the nanowire cavity. These images confirm the presence of waveguiding effects for core-shell ZnO nanowires and ensure directional emission for scintillator applications.

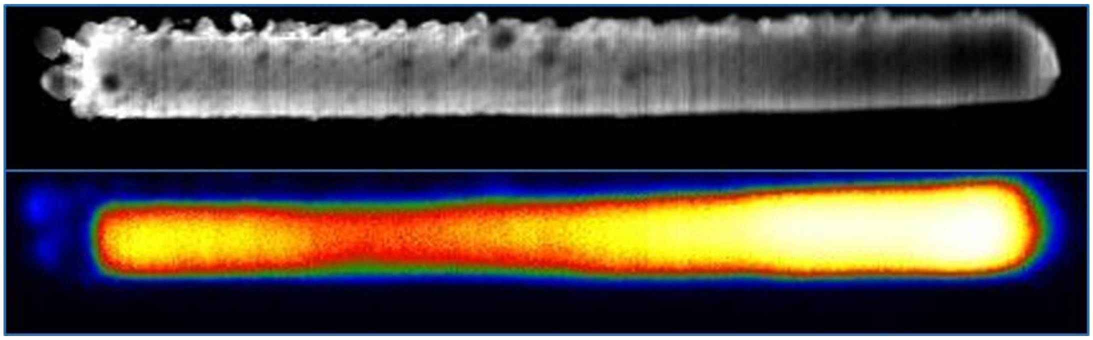

Figure 28: High-resolution HAADF and cathodoluminescence measurements, top and bottom respectively, of a ZnO-MgO core-shell nanowire more uniformly decorated with Ag nanoparticles. The emission is much brighter at the ends of the nanowire than in the center, verifying the presence of waveguiding effects.

CHAPTER 4

INITIAL EXPERIMENTS WITH ZNO NANOWIRE SCINTILLATORS

4.1 Irradiation Experiment

To study the effects of radiation on the luminescent properties of ZnO nanowires, a new nanowire sample was grown onto a fused silica substrate using the modified vapor-solid method described previously. Scanning electron micrographs of the sample were taken using a Zeiss Merlin high-resolution SEM to examine the nanowire morphology and uniformity, as seen in Figure 29. Image processing software was then used to estimate average nanowire diameters and lengths of 80-100 nm and 1-2 µm respectively. Moreover, photoluminescence measurements were taken at multiple locations across the sample to verify that the integrated intensities of both the band-edge and visible emission varied by less than 10%. These specific locations were then used in subsequent radiation experiments.

Photoluminescence spectra were then acquired both before and after irradiation using a 325 nm He-Cd laser in a Horiba LabRam HR800 system that showed an integrated band-edge emission intensity two orders of magnitude greater than that of the defect emission, indicating high crystallinity of the nanowires. The band-edge emission spectra were acquired with a 0.1 s accumulation time, while the visible emission required a 5.0 s accumulation time since the emission was much lower in intensity. At each point where PL spectra were acquired, the software looped through four repetitions and then constructed an average. For each selected location on the sample, PL spectra were acquired at the corners and the center of a square 0.2 mm on a side and were averaged to provide more accurate PL spectra that would be representative of the range of nanowire diameters and morphologies. The spectra shown in

Figure 29 are representative of the emission seen across the sample with less than 10% variation in the integrated areas for both the band-edge and visible emission, establishing this sample as suitable for comparative measurements.

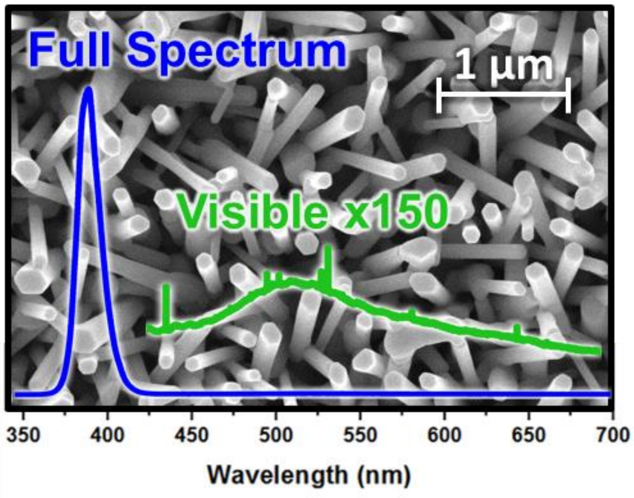

Figure 29: Scanning electron microscope image of ZnO nanowire sample. The nanowires are faceted, approximately 80-100 nm in diameter and 1-2 µm in length. Photoluminescence spectra taken at the same location show the high degree of crystallinity of the nanowires, with the band-edge exciton emission intensity approximately 150 times that of the visible defect emission.

Before each irradiation, the selected portion of the sample was masked using a 2.5 cm thick lead brick with a 5x7 mm rectangular notch aperture to minimize vignetting effects. The sample was then placed inside a J. L. Shepherd and Associates Mark I cesium irradiator at a distance approximately 2.5 cm away from an 84 TBq ^{137}Cs source. Cesium-137 is a mono-energetic emitter of 662 keV gamma rays, an energy close to the 511 keV gamma rays emitted during positron annihilation in PET scans. At the distance of 2.5 cm, the dose rate was measured to be 0.17 Gy/s = 0.17 J/kg/s ≈ 10^{18} eV/kg/s with an approximate flux of 1×10^{12} gamma rays per second per cm^2.

4.2 Radiation Damage Effects

4.2.1 Radiation Damage to Nanowires in Literature

Several investigations into the damage effects of gamma-ray irradiation on nanowires have been carried out over the last decade. The nanowires that have been studied primarily consist of metals and metal oxides since the methods of nanowire growth for these materials are already well established. The nanowire architecture has the potential to differ greatly from bulk crystals in its response to gamma rays due to the much larger surface-to-volume ratio and the high degree of crystallinity typically seen. Therefore, it is important to examine the overall effects of gamma-ray irradiation on nanowires before moving onto the ZnO nanowire experimental results.

In one study, the potential damage effects of gamma-ray radiation from a ^{137}Cs source on SnO_2 nanowires was examined[96]. Tin oxide nanowires were grown using a vapor-liquid-solid method with the results shown in Figure 30. The randomly aligned nanowires had an extremely high aspect ratio with an average diameter of 200 nm and a length of tens of microns. In addition, TEM images showed the high-crystallinity of the nanowires, providing an ideal system to study the effects of gamma-ray irradiation. Gamma rays of 662 keV energy from the ^{137}Cs source were used to irradiate the sample. Dosages varied from 5 mGy/hr to 420 mGy/hr at a distance between the sample and the cesium source of 365 cm and 40 cm respectively.

Resistance measurements were taken *in situ* and showed a 14.8 MΩ increase in resistance at the higher irradiations. This was attributed to a decrease in available charge carriers as the ionized and hot electrons were trapped by induced mid-gap, defect states, including singly- and

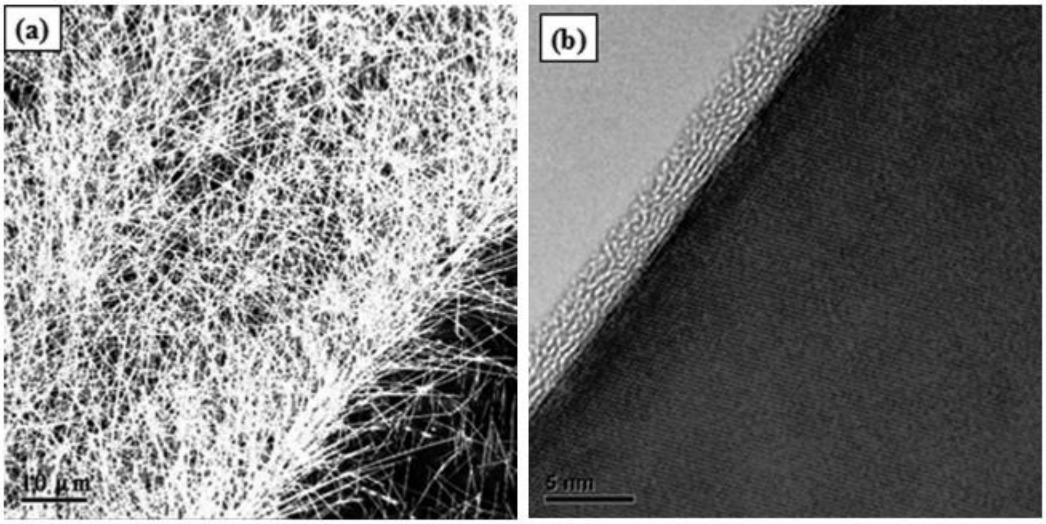

Figure 30: Carpet SnO_2 nanowires with high aspect ratios are shown in (a). High-resolution TEM image of a single nanowire with well-ordered growth planes visible in (b). This shows the highly crystalline nature of the nanowires[96].

doubly-charged oxygen vacancies. Photoluminescence measurements with a He-Cd 325 nm excitation source showed a large increase in the overall emission of the SnO_2 nanowires, as seen in Figure 31. The large emission increase was partly attributed to the luminescence of the created trap sites and was a result of total dosages of only 21 Gy and 42 Gy for the red and blue traces respectively. This illustrated how sensitive the SnO_2 nanowires were to 662 keV gamma rays. The singly-charged oxygen vacancy peak position is located at 590 nm and is greatly enhanced after 42 Gy of radiation. This enhancement was also attributed to the large number of hot electrons filling the trap sites.

In additional experiments, Zn[97], Cu[98], and Cd[99] nanowires were grown using an electro-deposition technique within a polycarbonate track-etch membrane with a pore size of 100 nm and 10 microns of thickness mounted onto a copper substrate. The polycarbonate was then

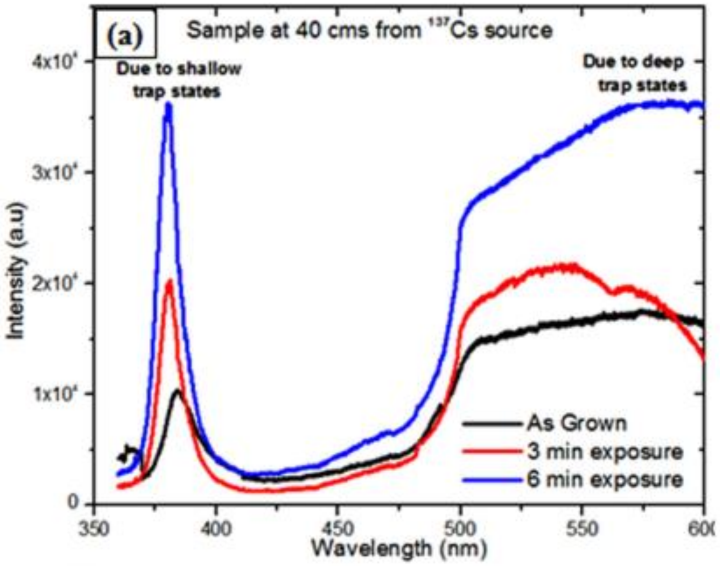

Figure 31: Photoluminescence measurements of 662 keV irradiated SnO_2 nanowires. The red and blue traces correspond to total dosages of 21 and 42 Gy respectively[96].

dissolved, leaving the Zn, Cu, and Cd nanowires as shown in Figure 32. The nanowires were all irradiated by a ^{60}Co source, which emits at 1.17 and 1.33 MeV. All of the nanowire samples showed a strong decrease in conductivity as a function of radiation dosage, which agreed with the effects seen in the SnO_2 nanowires. However, the dosage for the metal nanowires was much higher at 200 kGy, 250 kGy, and 100 kGy for the Zn, Cu, and Cd samples respectively. The authors stated that the mechanism behind the decrease in conductivity was a change in the grain sizes, boundaries, and orientations within the metal nanowires.

Finally, CeO_2 nanowires were grown via a hydrothermal method and irradiated by a ^{137}Cs source for dosages in the μGy range[100]. Figure 33 shows an SEM micrograph of the randomly oriented nanowires and transmittance spectra after irradiation. The nanowires showed a

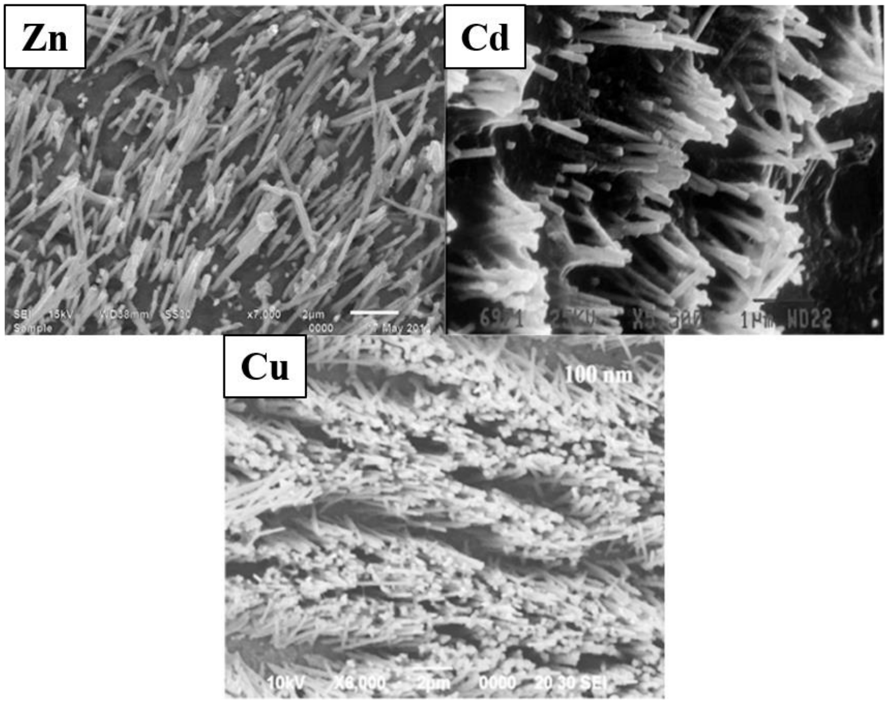

Figure 32: Scanning electron microscope images of Zn, Cu, and Cd nanowires grown by electrodepositing Zn within a polycarbonate trace-etch membrane. The polycarbonate was then dissolved, leaving the nanowires as shown[97-99].

transmittance response at dosage thresholds as low as 10 μGy, a sensitivity improvement of three orders of magnitude over chemical dosimeters. This study highlights how sensitive nanowires can be to gamma-ray irradiation and is in stark contrast to the radiation hardness of ZnO nanowires.

4.2.2 Radiation Damage to ZnO Nanowires

To examine the radiation effects on the ZnO nanowire structure, a 5x5 mm^2 section of the sample was irradiated for 10 hours for a total dosage of approximately 6000 Grays. Photoluminescence spectra were taken each day for three days with the sample held in dark conditions between measurements. The results are shown in Figure 34. The band-edge emission

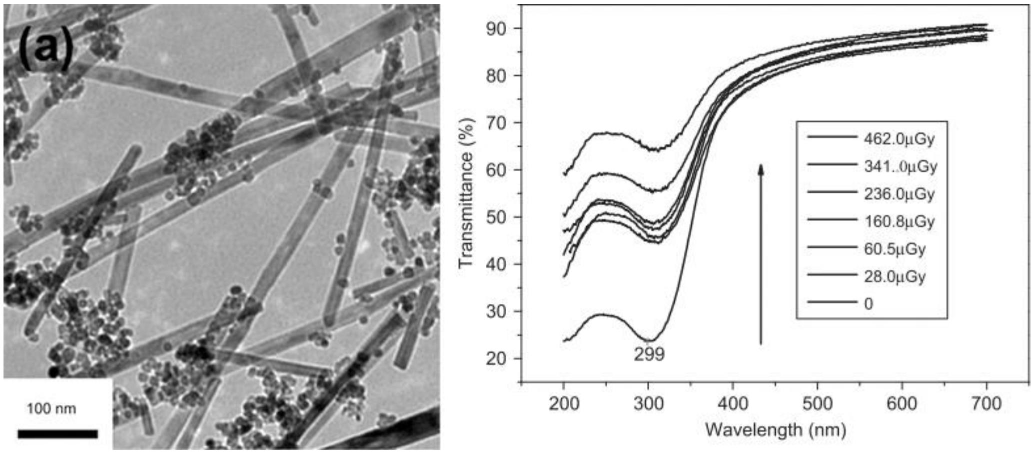

Figure 33: On the left, an SEM micrograph of CeO_2 nanowires grown via a hydrothermal method. On the right, transmittance spectra of the CeO_2 nanowires after irradiation from a ^{137}Cs source[100].

is relatively unaffected by the irradiation. Contrariwise, the visible emission shows a large amount of change. Using MATLAB to fit Gaussian curves to deconvolute the PL from discrete defects, resulted in two main peak locations, as seen in Figure 34. The first of two peaks, denoted by dashed lines, is located at 490 nm and corresponds to the singl charged oxygen vacancy, where an electron has been trapped in the potential well of the oxygen vacancy. The second peak, denoted by dotted lines, is centered at 510 nm and corresponds to the doubly charged oxygen vacancy; no electrons are present in such a defect site.

Figure 34 also shows the integrated intensities for the fitted Gaussians. Before irradiation, almost all of the oxygen vacancies are doubly charged. After irradiation, the overall amount of oxygen vacancies nearly doubles, with almost all of the emission corresponding to singly charged oxygen vacancies. Over a period of three days, the defect emission returns to pre-irradiation levels.

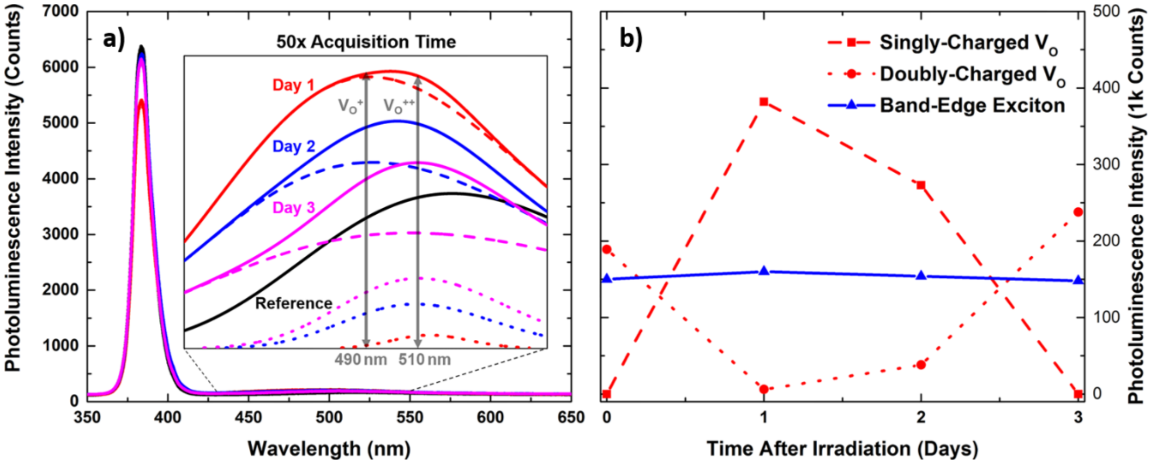

Figure 34: Room-temperature photoluminescence measurements taken each day for three days following irradiation of ZnO/MgO core-shell nanowires by 662 keV gamma rays. In (a), the peak centered at 380 nm corresponds to the band-edge exciton emission while the inset displays Gaussian fits for the visible emission. The dashed and dotted lines correspond to the fits for singly- and doubly-charged oxygen vacancy emissions respectively. In (b), the relative intensities for the singly- and doubly-charged oxygen vacancy emissions, as well as for the band-edge emission, are shown as a function of time.

The primary interaction for 662 keV gamma rays with the ZnO sample is through Compton scattering, in which the high-energy photons inelastically scatter from both electrons and nuclides. In the first case, electrons are initially ionized, but as the energy is gradually reduced through interactions, electrons are excited high into the conduction band and are referred

The displacement energies for oxygen and zinc in ZnO are 310 keV and 900 keV, respectively[101]. Therefore, the 662 keV gamma rays have enough energy to form oxygen vacancies within the lattice but not enough energy to form zinc vacancies. The doubly-charged oxygen vacancies then serve as trap sites for the hot electrons, resulting in the formation of F+ centers. When the color center relaxes, a singly-charged oxygen vacancy results. A schematic showing the energetics of gamma-ray interaction with the ZnO nanowires is shown in Figure 35.

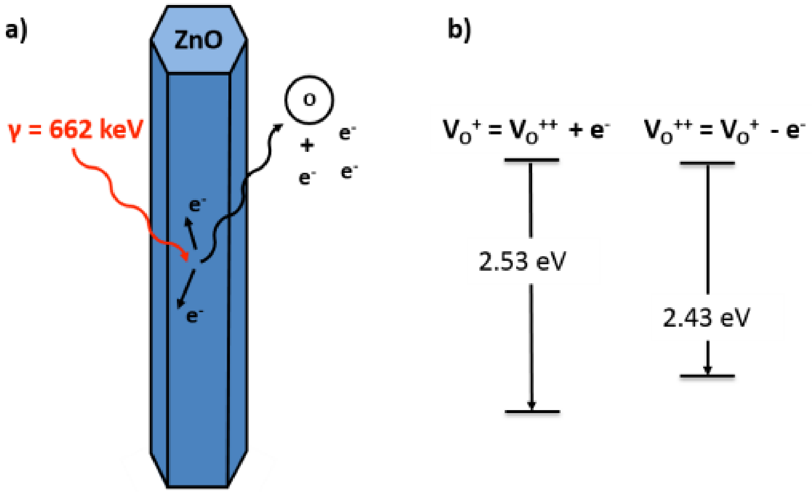

Figure 35: (a) Schematic of a ^{137}Cs gamma ray generating oxygen vacancies in the ZnO lattice in addition to ionization due to Compton scattering (b) Energy-level diagrams for singly- and doubly-charged oxygen vacancy emission.

The singly charged oxygen vacancies are thermodynamically unstable[39, 102], so over a period of days, electrons escape the trap sites. In addition, it is energetically favorable for oxygen vacancies to diffuse toward the surface of the very thin nanowires[103]. This self-annealing behavior is consistent with previous research[104] and returns the ZnO nanowires to a pre-irradiation state within a few days, illustrating the radiation hardness of highly crystalline ZnO.

4.3 Photoluminescence Yield

To estimate the scintillation efficiency in terms of photons detected as a function of energy deposited by the gamma rays, it is critical to understand how a ZnO nanowire scintillator would differ from a conventional one. In a typical scintillator, gamma rays are completely attenuated within an interaction volume of cm^3; photons emitted by electron-hole-pair recombination are counted in a photomultiplier, and the counts recorded over a given time are divided by the total deposited energy to yield a figure of merit in terms of *(Nhv)/*MeV. A good scintillator typically has a light yield of 10^4-10^5 photons/MeV, with high-quality, undoped ZnO ceramic scintillators having a light yield around 9 x 10^4 photons/MeV[45].

In the nanowire system, an analogous method may be used with the photoluminescence yield. However, only a small fraction of the irradiated nanowires, corresponding to the focal volume of the PL pump laser, is responsible for the photoluminescence. In PL measurements, the laser spot size was approximately 10 µm in diameter, while the overall nanowire coverage was 0.08, as estimated from SEM images. This, combined with an average nanowire length of 1.5 µm, gives a PL excitation volume of approximately 10 µm^3. By multiplying the excitation volume by the density of ZnO, 5.6 g/cm^3, we obtain roughly 5 x 10^{-14} kg for the total mass of ZnO excited by the PL pump laser.

For 662 keV gamma rays, the mass attenuation coefficient for ZnO was interpolated from recent literature[105] to be approximately 7.45 x 10^{-2} cm^2/g, thereby yielding a linear attenuation coefficient of 0.418 cm^{-1}. Invoking Beer's law given the average nanowire length of 1 µm gives a fractional absorbed intensity of the gamma-ray beam of order 6 x 10^{-5} of the incident beam. This gives an overall light yield of:

$$\Phi = \frac{\frac{N_{PL}(h\nu)}{s}}{absorbed\ \gamma\ rate\ \left({}^{eV}\!/_{s}\right)}\ in\ irradiated\ volume \tag{17}$$

$$\Phi = \frac{7.6\times10^4\,\frac{counts}{s}}{\left(0.17\,\frac{Gy}{s}\right)\times(3.6\times10^5 s)\times(6\times10^{-5})\times(5\times10^{-14}\ kg)\left(6.24\times\frac{10^{12}MeV}{J}\right)} \tag{18}$$

$$\Phi \cong \boldsymbol{6\times10^5\,\frac{\frac{counts}{s}}{MeV}} \tag{19}$$

This remarkably high yield suggests that the ZnO nanowire system has the potential to be sensitive to a total dose at least two orders of magnitude less than that used in this initial study. This is somewhat surprising given that the stopping power of ZnO and interaction volume are so much lower than traditional scintillators. However, the high crystallinity of the nanowires combined with the wave-guiding efficiency has the potential to explain the high photoluminescence response. In the nanowire system, the entire volume of each nanowire can potentially contribute to the photon yield by creating optically active defects and subsequent defect luminescence, whereas in conventional scintillators the small concentration and relatively low quantum yields of the activator dopants (typically rare-earth atoms) can dramatically reduce the effective volume in which observable emissions eventually take place. Moreover, the wave-guiding effect of the ZnO nanowires ensures an essentially unidirectional photon emission for detection, resulting in a highly efficient overall process.

4.4 Dosage Effects

To study the effects of different dosages of 662 keV radiation on ZnO nanowires, a new sample was grown using the modified vapor-solid method outlined previously. The sample was again characterized via SEM imaging to verify the presence of uniform nanowire growth, and PL measurements were taken to identify locations with band-edge and visible emission peak intensities with less than 10% variance. The sample was masked with a lead brick as before and irradiated for 10 hours for a dosage of approximately 6000 Gy. After this, PL measurements were taken at the irradiated location, but little change in both the band-edge and visible emission was observed as seen in Figure 36.

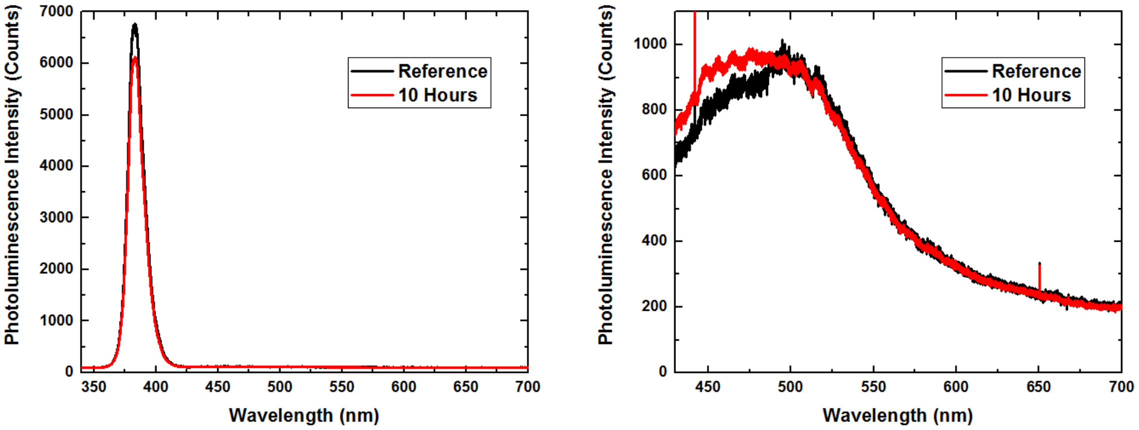

Figure 36: Photoluminescence spectra for the masked ZnO nanowire sample before and after ten hours of irradiation. On the left, the band-edge emission is shown to slightly decrease after the irradiation. On the right, the visible emission line shape broadens slightly toward the blue edge of the resonance, indicating an increase in singly-charged oxygen vacancies.

The intensity changes for the visible emission were much smaller than those observed in the previous time-dependent measurements of radiation damage. This inconsistency could be potentially explained by a slightly offset or angled lead mask. Since the rectangular aperture was 5 mm in width and 25 mm in depth, even a small change in the angle or position of the mask relative to the cesium source could produce strong attenuation effects. To remove any possibility of masking error, a new set of measurements were taken using a different protocol.

The sample was mounted onto a new optical slide that was then attached to the lead brick base at the same height as before, but without any lead mask. The sample was irradiated for one hour for a dosage of approximately 600 Gy and immediately followed by PL measurements. The sample was then irradiated for four more hours for a dosage of approximately 2400 Gy and a total dosage of 3000 Gy that should be equivalent to irradiating for five hours. After the four-hour irradiation, PL measurements were repeated. Five more hours of irradiation followed for a total dosage of 6000 Gy that should be equivalent to irradiating for ten hours. To minimize any self-annealing effects, the sample was only exposed to light when transferring to and from the irradiation chamber. At all other times, the sample was kept in a dark environment. In summary, the PL measurements were taken for total dosages that corresponded to 600, 3000, and 6000 Gy. This method not only eliminated any potential masking and positioning errors, but controlled for the slight variations present between locations on the sample. Furthermore, the color of the optical slide changed to an amber color, indicative of F-center generation, that confirmed the sample was exposed to large doses of gamma radiation.

The PL measurements taken during this unmasked series are shown in Figure 37.

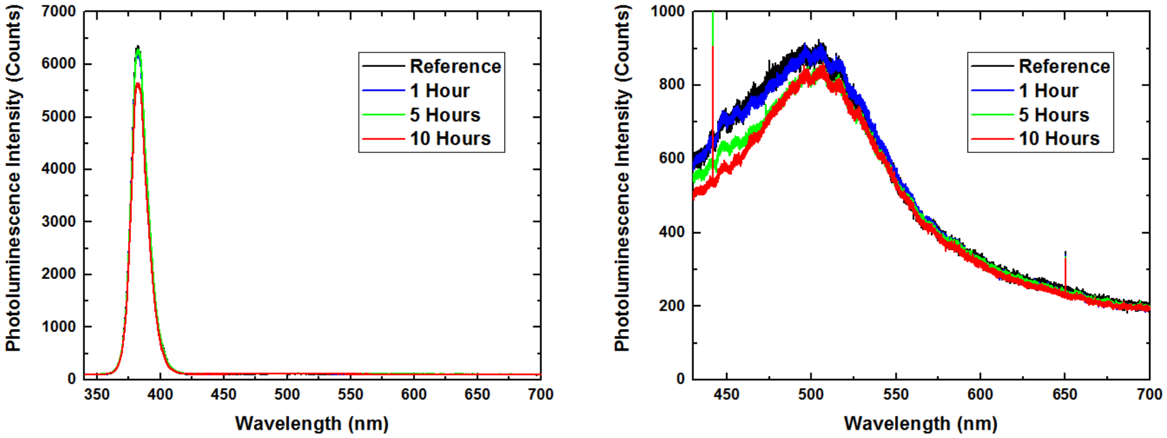

Figure 37: Photoluminescence measurements of the unmasked ZnO nanowire sample after one, five, and ten hours of irradiation. On the left, the band-edge emission shows a decrease in intensity only after 10 hours of irradiation On the right, the visible emission line shape narrows slightly, indicating a decrease in singly-charged oxygen vacancies.

The intensity changes in the visible emission were again much smaller than expected, but were consistent in magnitude with the spectra seen in Figure 36. The difference between the two ten-hour irradiations was a narrowing of the line shape for the sequentially irradiated sample. Figure 38 shows a zoomed-in perspective of the spectra shown above. The band-edge emission shows a drop in intensity for the 10-hour irradiation, but seems unaffected for the 1- and 5-hour irradiations. The visible emission shows a drop in overall intensity for the 5- and 10-hour irradiations with a slight narrowing of the line shape. The narrowing is more pronounced for the 10-hour irradiation.

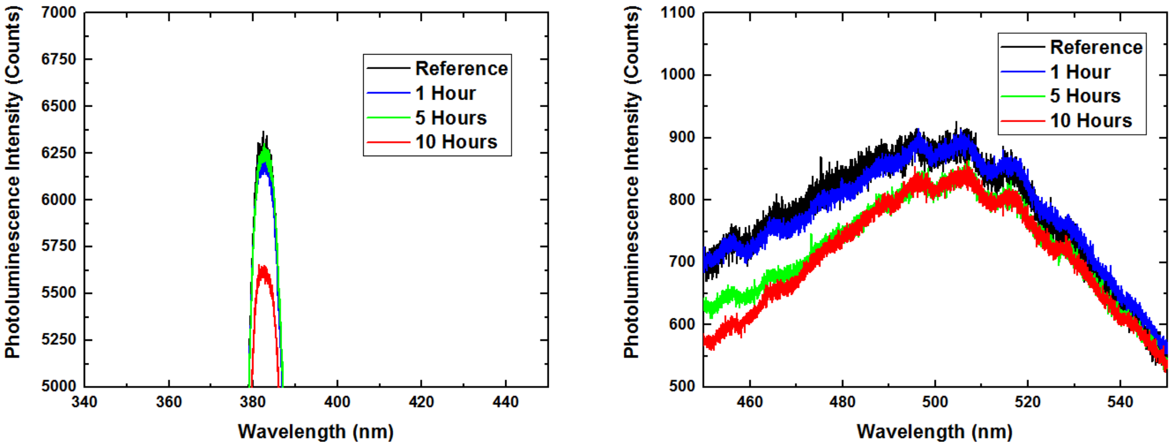

Figure 38: Zoomed-in view of PL spectra in Figure 37. On the left, the band-edge emission shows a significant reduction in intensity for the ten-hour irradiation. On the right, the visible emission shows a slight decrease in intensity for the five- and ten-hour irradiations. In addition, the line shape appears to narrow for the ten-hour irradiation.

Comparing the visible emissions of the 10-hour irradiations for the masked and unmasked samples shows an increase in singly-charged oxygen vacancies for the masked sample versus a decrease in singly-charged oxygen vacancies for the unmasked sample. One possible explanation is that repeated PL measurements of the same location on the unmasked sample imparted enough energy to accelerate the self-annealing effect seen in the time-dependent measurements.

To test this hypothesis, PL measurements were taken sequentially at a location on the time-dependent sample without moving the sample or turning off the laser beam. Each measurement took approximately eleven minutes for a total irradiation time of fifty-five minutes. The PL measurements are shown in Figure 39. The spectra show very little variance, confirming that repeated PL measurements at the same location were unlikely to be the source of the line-shape change. Two possible causes are the extra exposure to light when mounting and unmounting the sample in the irradiation chamber and the extra thermal energy absorbed from transporting the sample between Vanderbilt University, where the irradiations were performed, and Fisk University, where the PL measurements were taken.

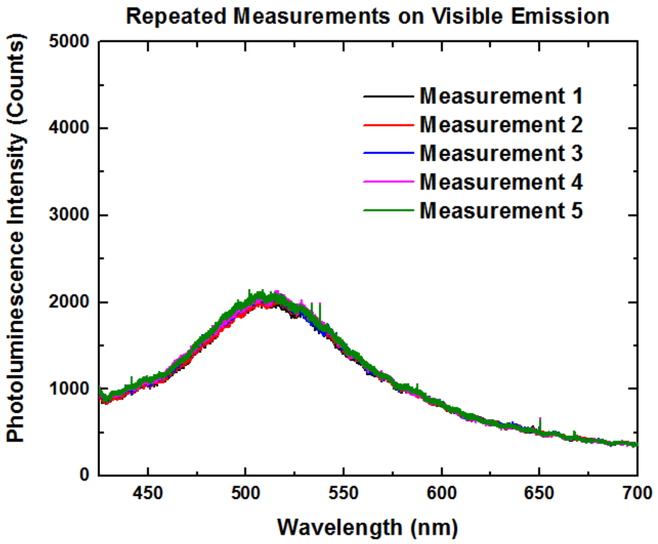

Figure 39: Repeated PL measurements at the same location on the time-dependent ZnO nanowire sample. This shows that taking sequential PL measurements does not appear to cause changes in the visible emission.

There was a substantial difference in the visible emission response to irradiation between the time-dependent sample, shown in Figure 34, and the dose-dependent sample, shown in Figure 37. For the time-dependent sample, the total visible emission almost doubled, while the visible emission for the dose-dependent sample slightly decreased. One explanation for this difference is the potential physical difference between the two nanowire samples. They were grown using the same protocol, but differences in nanowire morphologies and PL responses are common between samples. The different PL responses can reflect different defect loads within the nanowires and have the potential to result in greatly differing responses to radiation effects.

However, one feature consistenly seen across both samples, and for both the masked and unmasked locations, was the approximately 10% drop in band-edge emission intensity after ten hours of irradiation. For the time-dependent sample, this drop could correspond to the increase in radiative defects, both singly- and doubly-charged oxygen vacancies. For the dose-dependent sample, the decrease in the band-edge emission could correspond to an increase in non-radiative defects; the presence of additional non-radiative defect sites would also help explain the large difference in the visible emission response to irradiation.

4.5 Time-Resolved Photoluminescence

Time-resolved photoluminescence (TRPL) measurements were taken for the band-edge emission of a ZnO nanowire sample using a custom Halcyone fluorescence and second harmonic generation system shown in Figure 40. A 10 W Verdi G 532 nm laser was used to pump a 78 MHz, 150 fs, 10 nJ Ti:Sapphire laser oscillator (Coherent Mira 900). For the pump/probe measurement, the 800 nm fundamental from the Ti:Sapphire laser was split into two beams. One beam was used as a pump to excite the sample while the other beam was used to probe the photoluminescence response at 1.0 ps time steps that were generated from small changes in the path length of the probe beam.

The third harmonic of the pump beam, at 266 nm, was used to excite the ZnO nanowire sample and was subsequently filtered out using a band pass filter. The 380 nm band-edge

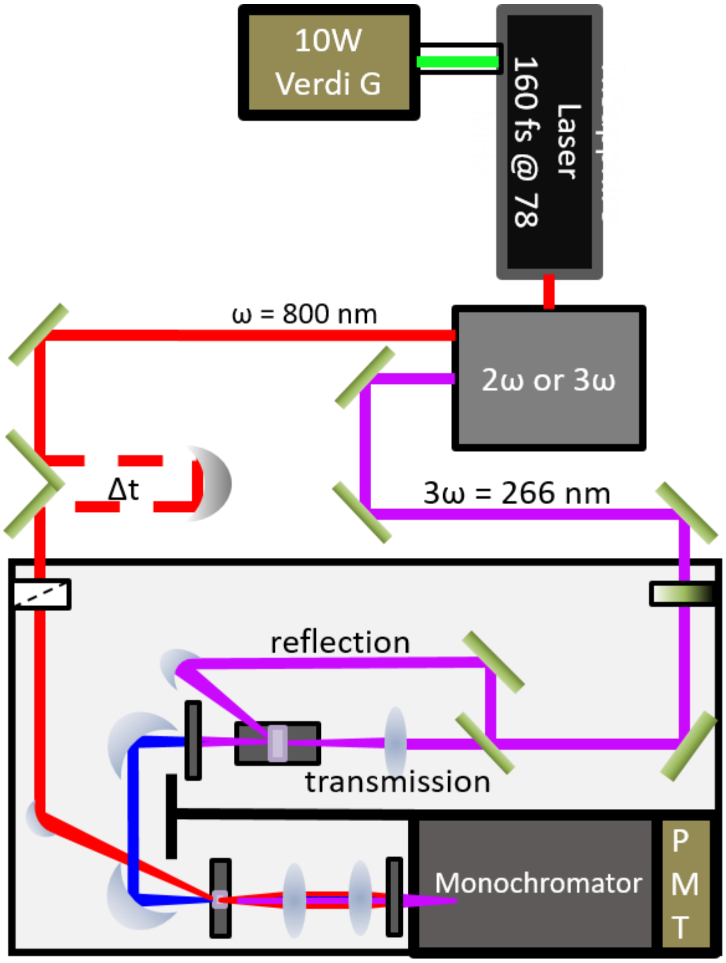

Figure 40: Custom-built Halcyone fluorescence and second harmonic generation system with a 78 Mhz, 150 fs, 10 nJ Ti:Sapphire laser pumped by a 10W Verdi 532 nm laser.

emission from the ZnO nanowires and the 800 nm probe beam were focused on a BBO crystal to generate the sum frequency at 258 nm. A mid-UV band pass filter was used to filter the 258 nm signal before the monochromator and photomultiplier tube that was used to amplify the signal. This measurement was repeated for ten scans of 200 ps duration, spaced out over 0.5 seconds total time, and averaged. For the next time step, the optical path length of the probe beam was increased by approximately 150 µmto increase the time for the probe beam to reach the BBO crystal by 1 ps. This process was then repeated to generate the time-resolved photoluminescence data seen in Figure 41.

A bi-exponential equation of the form,

$$y = y_0 + A_1 e^{-t/\tau_1} + A_2 e^{-t/\tau_2} \qquad (20)$$

was used to fit the data where the time constants τ_1 and τ_2 were found to be 70.5 ± 30.2 ps and 10.2 ± 4.1 ps respectively. The 70 ps time constant corresponds to the response from the bulk within the ZnO nanowires while the 10 ps time constant corresponds to the surface response and is approximately an order of magnitude faster since the excitons are less tightly bound at the surface.

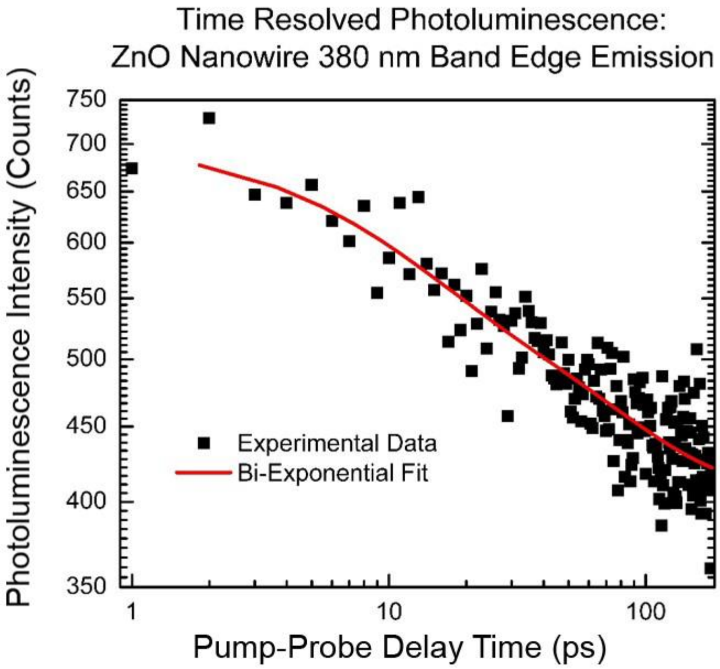

Figure 41: Time-resolved photoluminescence measurements of the band-edge emission of ZnO nanowires. The bi-exponential fit found two time constants. The first one was 70 ps and corresponded to the bulk of the nanowires. The second was 10 ps and corresponded to the surface response.

This lifetime is much faster than the state-of-the-art LYSO scintillator crystals currently used in PET scan systems. The LYSO time resolution is 200 ps while the ZnO nanowire temporal resolution is an order of magnitude faster. This should directly translate to an improvement in PET scan image resolution from single-digit cm to single-digit mm, potentially providing unmatched accuracy in both cancer diagnosis and prognosis.

Time-resolved measurements of the visible emission of ZnO nanowires could not be taken on the Halcyone system since the signal was so weak. The band-edge emission itself was close to the threshold of distinguishing the signal from the noise. Since the visible emission is two orders of magnitude lower than the band-edge photoluminescence, it was not possible to acquire visible emission spectra. In any case, the lifetime of the visible photoluminescence is known to be of order nanoseconds, and the third harmonic of a pulsed Nd:YAG laser (355 nm) might well be a simpler choice for monitoring the visible luminescence directly.

CHAPTER 5

CONCLUSIONS

5.1 Discussion

Initial experiments have demonstrated that the ZnO nanowire system provides a radiation-hardened environment for gamma-ray scintillation. After being irradiated with approximately 6000 Grays from a 662 keV source, there were only two relatively minor changes to the photoluminescence. For the band-edge emission, a 10% drop in emission intensity was seen. For the visible emission, the generation of a large number of F^+ centers occurred within one sample while another was only slightly affected. Under dark conditions, the system then self-annealed within a few days to return back to baseline band-edge and visible emission.

The irradiated ZnO nanowire material also showed a photoluminescence efficiency on the order of 6×10^5 photons/MeV. This light yield illustrates the high radiative efficiency of the nanowires, which is critical given the low gamma-ray flux of $2 \times 10^4\ \gamma s^{-1} cm^{-2}$ in a typical PET scan system. The high crystallinity and waveguiding effects of the ZnO nanowires have the potential to overcome the disadvantages of low gamma-ray stopping power and extremely small interaction volume. Essentially, a large percentage of the light that is generated within the nanowires is unidirectionally emitted toward the detector, resulting in a highly efficient overall process. In order to further enhance the directionality of the emission, completely vertically aligned nanowires can be grown using a GaN substrate; the ZnO nanowires have less than a 2% lattice mismatch with GaN[106, 107] along the c-axis and thus grow normal to the substrate as shown in Figure 42.

The true potential of the ZnO nanowire scintillator system, however, is in its unique ability to decouple the two main components of scintillation: stopping power and detection efficiency. The overall stopping power of the system can be enhanced by intercalating a high-Z matrix material within the ZnO nanowires as shown in Figure 42. With this addition, some of the energy of incident gamma rays will be attenuated, leading to increased interaction with the ZnO nanowires. This system also allows for metal nanoparticles to be dispersed within the matrix material to examine plasmonic enhancement effects.

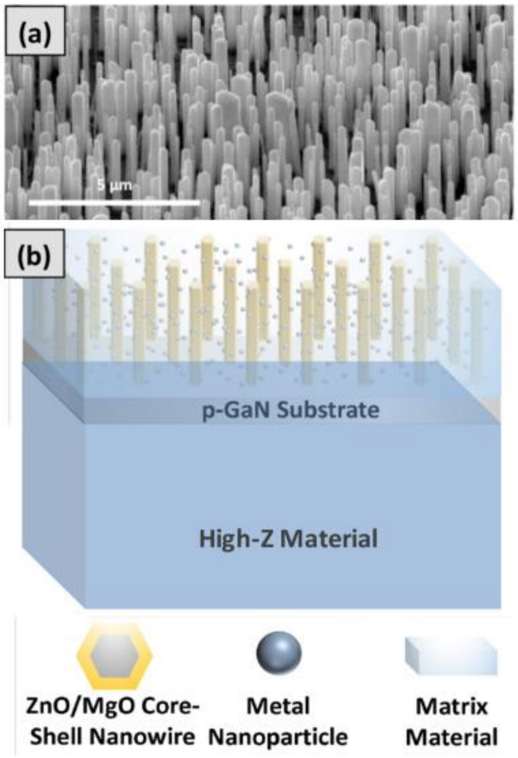

Figure 42: (a) Scanning electron microscope image of vertically-aligned ZnO nanowires grown via a hydrothermal method on a p-GaN substrate. (b) Schematic for an optimized nanowire scintillator: ZnO-MgO core-shell, vertical nanowires intercalated with a high-Z matrix material and plasmonic nanoparticles with a high-Z backing material to attenuate gamma-ray energy.

Furthermore, a layer of high-Z material may serve as a backing layer for the ZnO nanowires. The thickness of the layer can be optimized to attenuate the energy of the incident gamma rays before reaching the ZnO nanowires. This has the potential to greatly increase the interaction of the gamma rays with the nanowires, particularly if energy can be lowered to the level where the photoelectric effect dominates the photoelectron production dynamics. Increasing the interaction cross section of the gamma rays with the ZnO nanowires is of critical importance since this capability will magnify the emission efficiency.

Detection efficiency can also be strongly modified with several emission-enhancement tools. Core-shell nanowires have been demonstrated to enhance the band-edge emission by a factor of fifteen, while plasmonic effects from the addition of silver nanoparticles have been shown to provide a further enhancement factor of three. Finally, vertically-aligned nanowires provide waveguiding for the emission that is directly in line with the detector, thus avoiding the strong loss of signal that can occur using conventional unidirectional scintillators.

The ability to decouple and separately optimize both the stopping power and the emission efficiency provides a unique detector concept and an experimental workbench that has the potential to systematically advance toward the goal of developing an optimized PET scan scintillator with unprecedented temporal and spatial resolution.

APPENDIX

A. COMSOL Parameters and Settings

Included in this appendix are all of the parameters and settings used to simulate the effects of an incident-plane-wave light source upon a core-shell ZnO-MgO nanowire. In this example, the light source wavelength is 380 nm and the nanowire diameter is 90 nm. Screenshots of the COMSOL program have been included throughout this appendix. In some cases, Photoshop was used to assemble multiple screen elements into a single graphic. However, no image editing was performed. Each section header in this appendix corresponds to an analogous section within the Model Builder of COMSOL with empty sections denoting no changes were made from the default settings.

1. GLOBAL

1.1 Definitions

1.1.1 Parameters

All of the parameters used to define the simulation are included in the graphic below. The lambda0 variable represented the wavelength of the incident plane wave, while tZ and tM represented the thickness of the nanowire and coating respectively. The n_ZnO and n_MgO variables defined the refractive index of ZnO and MgO for the given lambda0 and were used to calculate the effective refractive index, n_eff, of the core-shell nanowire. The variable R_Hex, and R_MgO, was defined to represent the "radius" of the nanowire – or the distance from corner to corner, while R_ZnO was the distance of the ZnO core from corner to corner. These "radii" were used to define the vertices of the hexagonal polygons *(pol1, pol2)* in the model.

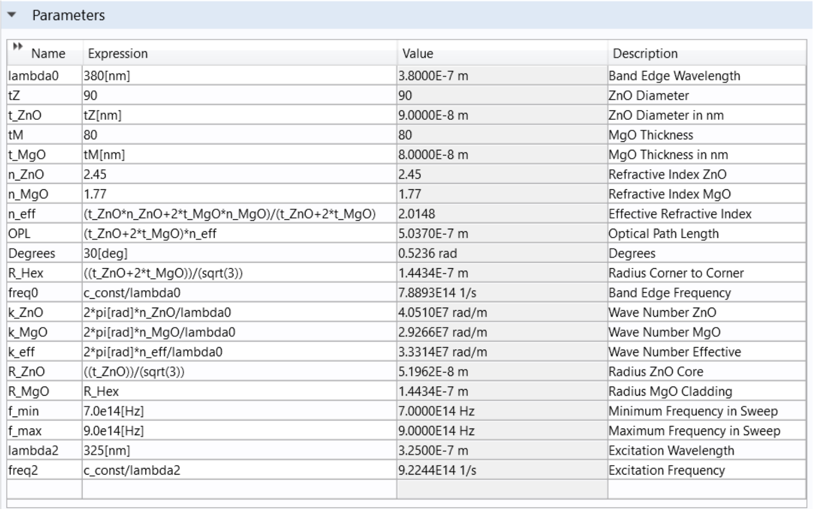

Name	Expression	Value	Description
lambda0	380[nm]	3.8000E-7 m	Band Edge Wavelength
tZ	90	90	ZnO Diameter
t_ZnO	tZ[nm]	9.0000E-8 m	ZnO Diameter in nm
tM	80	80	MgO Thickness
t_MgO	tM[nm]	8.0000E-8 m	MgO Thickness in nm
n_ZnO	2.45	2.45	Refractive Index ZnO
n_MgO	1.77	1.77	Refractive Index MgO
n_eff	(t_ZnO*n_ZnO+2*t_MgO*n_MgO)/(t_ZnO+2*t_MgO)	2.0148	Effective Refractive Index
OPL	(t_ZnO+2*t_MgO)*n_eff	5.0370E-7 m	Optical Path Length
Degrees	30[deg]	0.5236 rad	Degrees
R_Hex	((t_ZnO+2*t_MgO))/(sqrt(3))	1.4434E-7 m	Radius Corner to Corner
freq0	c_const/lambda0	7.8893E14 1/s	Band Edge Frequency
k_ZnO	2*pi[rad]*n_ZnO/lambda0	4.0510E7 rad/m	Wave Number ZnO
k_MgO	2*pi[rad]*n_MgO/lambda0	2.9266E7 rad/m	Wave Number MgO
k_eff	2*pi[rad]*n_eff/lambda0	3.3314E7 rad/m	Wave Number Effective
R_ZnO	((t_ZnO))/(sqrt(3))	5.1962E-8 m	Radius ZnO Core
R_MgO	R_Hex	1.4434E-7 m	Radius MgO Cladding
f_min	7.0e14[Hz]	7.0000E14 Hz	Minimum Frequency in Sweep
f_max	9.0e14[Hz]	9.0000E14 Hz	Maximum Frequency in Sweep
lambda2	325[nm]	3.2500E-7 m	Excitation Wavelength
freq2	c_const/lambda2	9.2244E14 1/s	Excitation Frequency

1.2 Materials - Default

2. MODEL

2.1 Definitions

2.1.1 Boundary System - Default

2.1.2 Perfectly Matched Layer

Perfectly matched layers (PML) were chosen for the top and bottom boundaries in our model to minimize scattering. At incident angles greater than 20° PMLs are recommended over scattering boundary conditions.

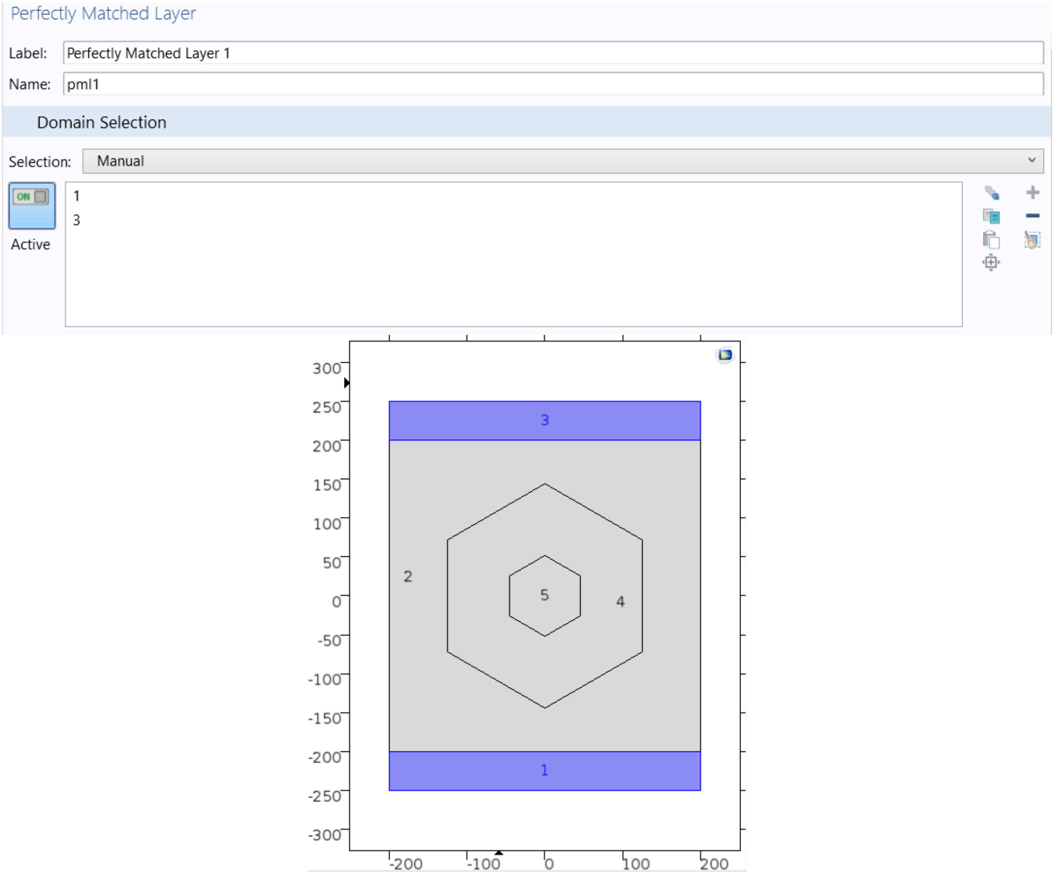

Perfectly Matched Layer

Label: Perfectly Matched Layer 1

Name: pml1

Domain Selection

Selection: Manual

1
3

2.1.3 View – Default

2.2 Geometry

The geometry for the model includes a hexagonal polygon for the ZnO core (*pol1*) and the MgO shell (*pol2*), two rectangles, (*r2*) and (*mir1*), for the PMLs, and an overall rectangle (*r3*) to provide the boundary for the excitation source and the scattering boundary condition (for low-angle scattering).

2.2.1 Polygon 1 (pol1)

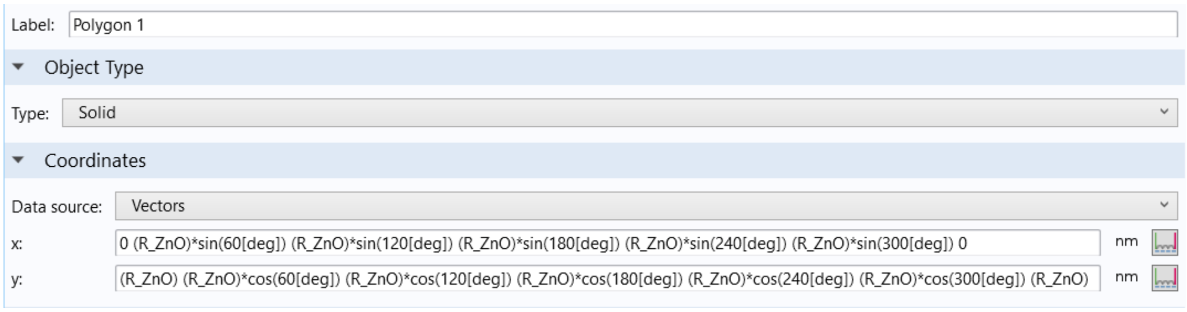

Label: Polygon 1

Type: Solid

Data source: Vectors

x: 0 (R_ZnO)*sin(60[deg]) (R_ZnO)*sin(120[deg]) (R_ZnO)*sin(180[deg]) (R_ZnO)*sin(240[deg]) (R_ZnO)*sin(300[deg]) 0 nm

y: (R_ZnO) (R_ZnO)*cos(60[deg]) (R_ZnO)*cos(120[deg]) (R_ZnO)*cos(180[deg]) (R_ZnO)*cos(240[deg]) (R_ZnO)*cos(300[deg]) (R_ZnO) nm

2.2.2 Rectangle 2 (r2)

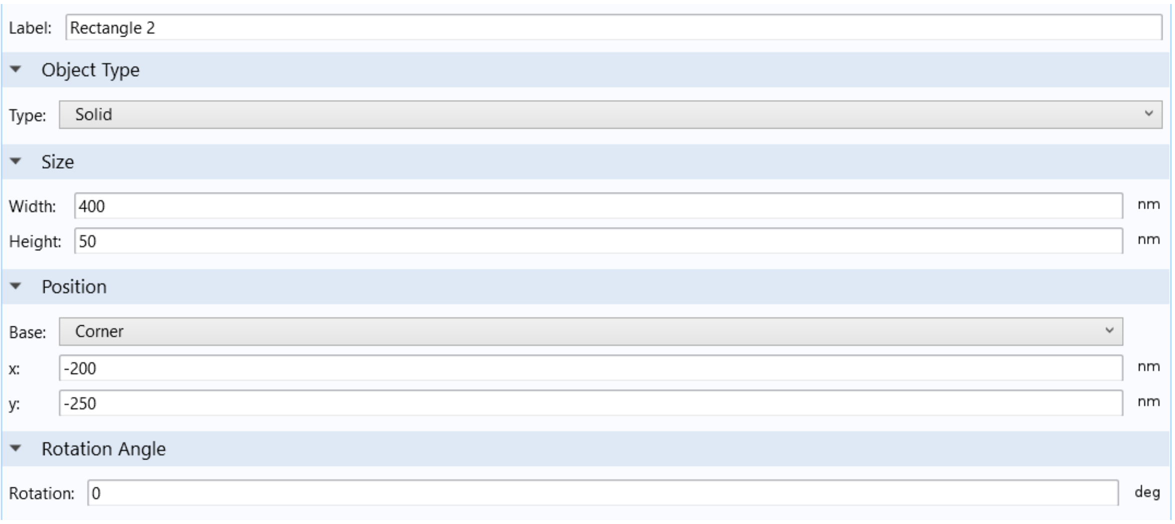

Label: Rectangle 2

Type: Solid

Width: 400 nm

Height: 50 nm

Base: Corner

x: -200 nm

y: -250 nm

Rotation: 0 deg

2.2.3 Polygon 2 (pol2)

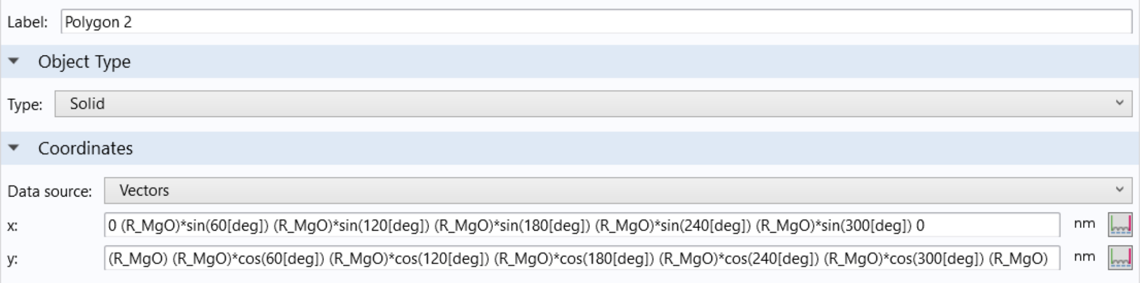

Label: Polygon 2

Object Type

Type: Solid

Coordinates

Data source: Vectors

x: 0 (R_MgO)*sin(60[deg]) (R_MgO)*sin(120[deg]) (R_MgO)*sin(180[deg]) (R_MgO)*sin(240[deg]) (R_MgO)*sin(300[deg]) 0 nm

y: (R_MgO) (R_MgO)*cos(60[deg]) (R_MgO)*cos(120[deg]) (R_MgO)*cos(180[deg]) (R_MgO)*cos(240[deg]) (R_MgO)*cos(300[deg]) (R_MgO) nm

2.2.4 Mirror 1 (mir1)

Label: Mirror 1

Input

Input objects:

r2

☑ Keep input objects

Point on Line of Reflection

x: 0 nm

y: 0 nm

Normal Vector to Line of Reflection

x: 0

y: 1

2.2.5 Rectangle 3 (r3)

Label: Rectangle 3

Object Type

Type: Solid

Size

Width: 400 nm

Height: 400 nm

Position

Base: Center

x: 0 nm

y: 0 nm

Rotation Angle

Rotation: 0 deg

2.3 Materials

The materials used for the simulation include the default air material for all domains other than the nanowire, a user-defined ZnO material for the ZnO core, and a user-defined MgO material for the MgO coating. The zinc oxide and magnesium oxide were user-defined in order to specify the wavelength dependent refractive index for 325 nm (the excitation wavelength) and 380 nm (the band-edge emission).

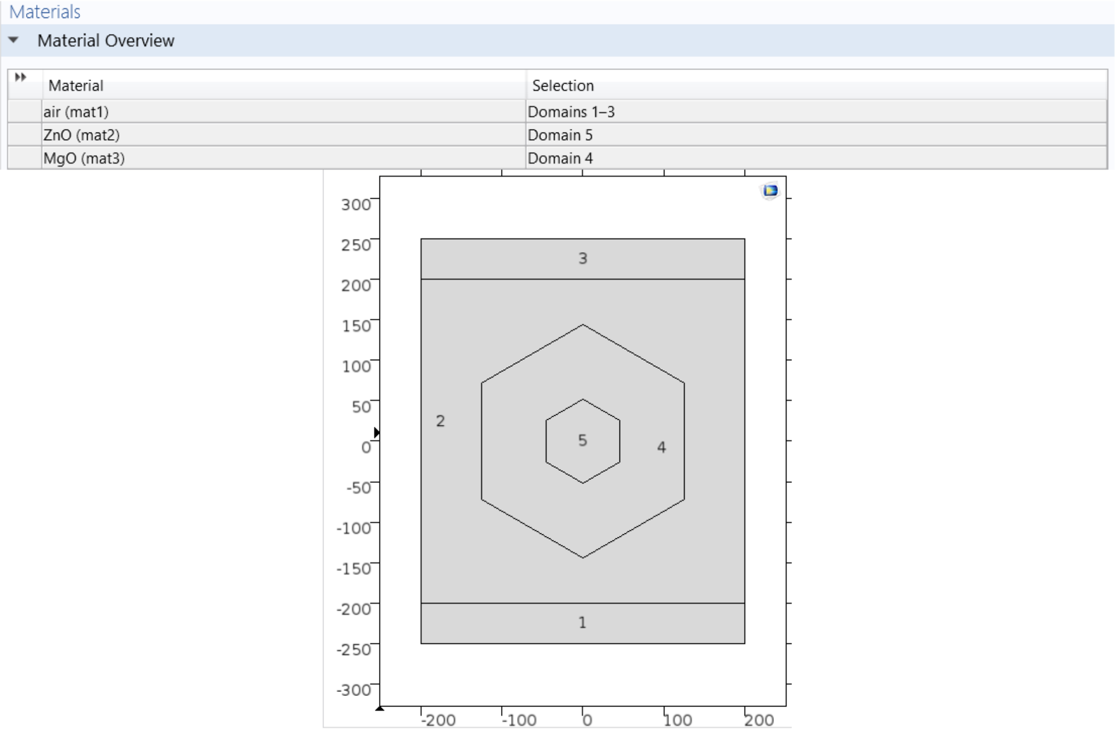

Material	Selection
air (mat1)	Domains 1–3
ZnO (mat2)	Domain 5
MgO (mat3)	Domain 4

2.3.1 Air

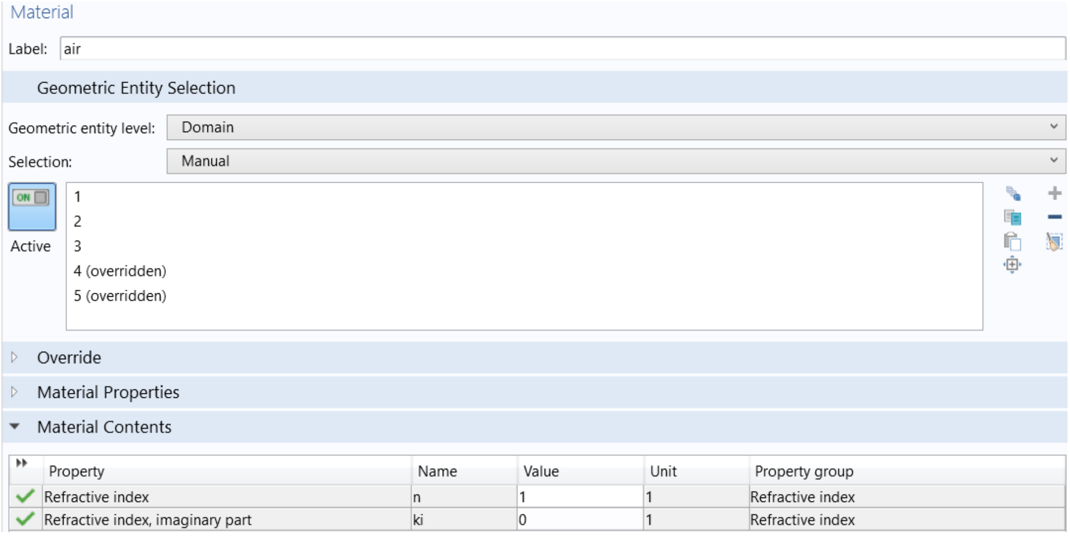

Material

Label: air

Geometric Entity Selection

Geometric entity level: Domain

Selection: Manual

Active

1
2
3
4 (overridden)
5 (overridden)

Override

Material Properties

Material Contents

	Property	Name	Value	Unit	Property group
✓	Refractive index	n	1	1	Refractive index
✓	Refractive index, imaginary part	ki	0	1	Refractive index

2.3.2 ZnO

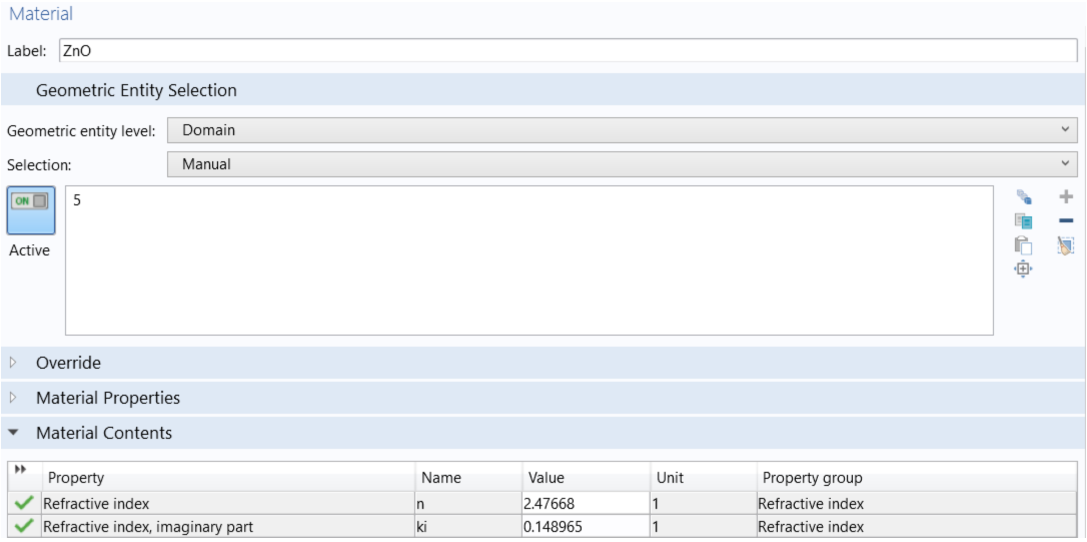

Material

Label: ZnO

Geometric Entity Selection

Geometric entity level: Domain

Selection: Manual

Active

5

Override

Material Properties

Material Contents

	Property	Name	Value	Unit	Property group
✓	Refractive index	n	2.47668	1	Refractive index
✓	Refractive index, imaginary part	ki	0.148965	1	Refractive index

2.3.3 MgO

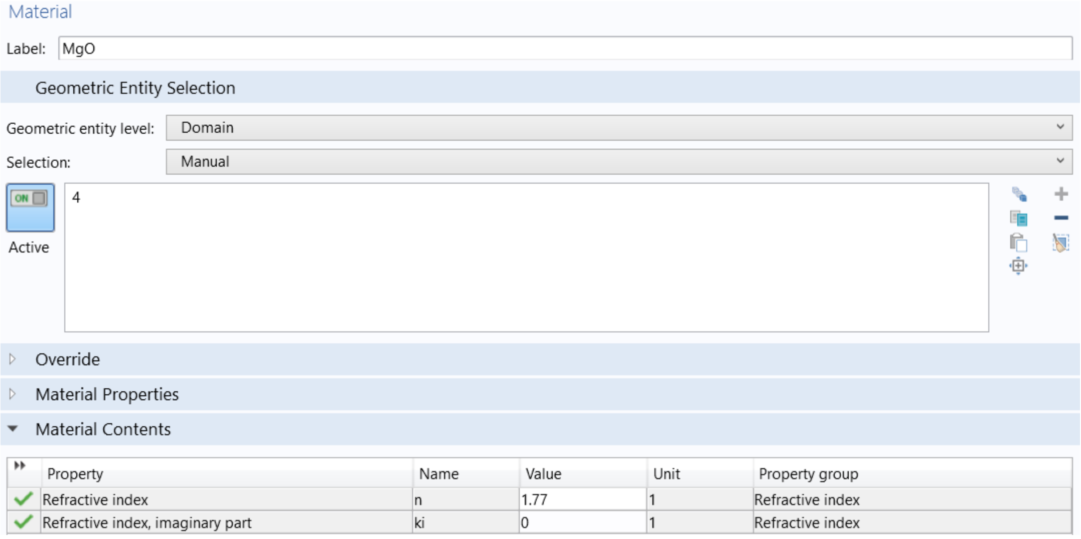

Label: MgO

Geometric entity level: Domain

Selection: Manual

4

Property	Name	Value	Unit	Property group
✓ Refractive index	n	1.77	1	Refractive index
✓ Refractive index, imaginary part	ki	0	1	Refractive index

2.4 Electromagnetic Waves, Frequency Domain

The scattering boundary conditions were defined within this section of the Model Builder. All exterior boundaries are defined as scattering boundary conditions to minimize low-angle scattering. Scattering Boundary Condition 2 also acts as the source of the plane-wave light source with an electric field strength of 1 V/m.

2.4.1 Scattering Boundary Condition 1

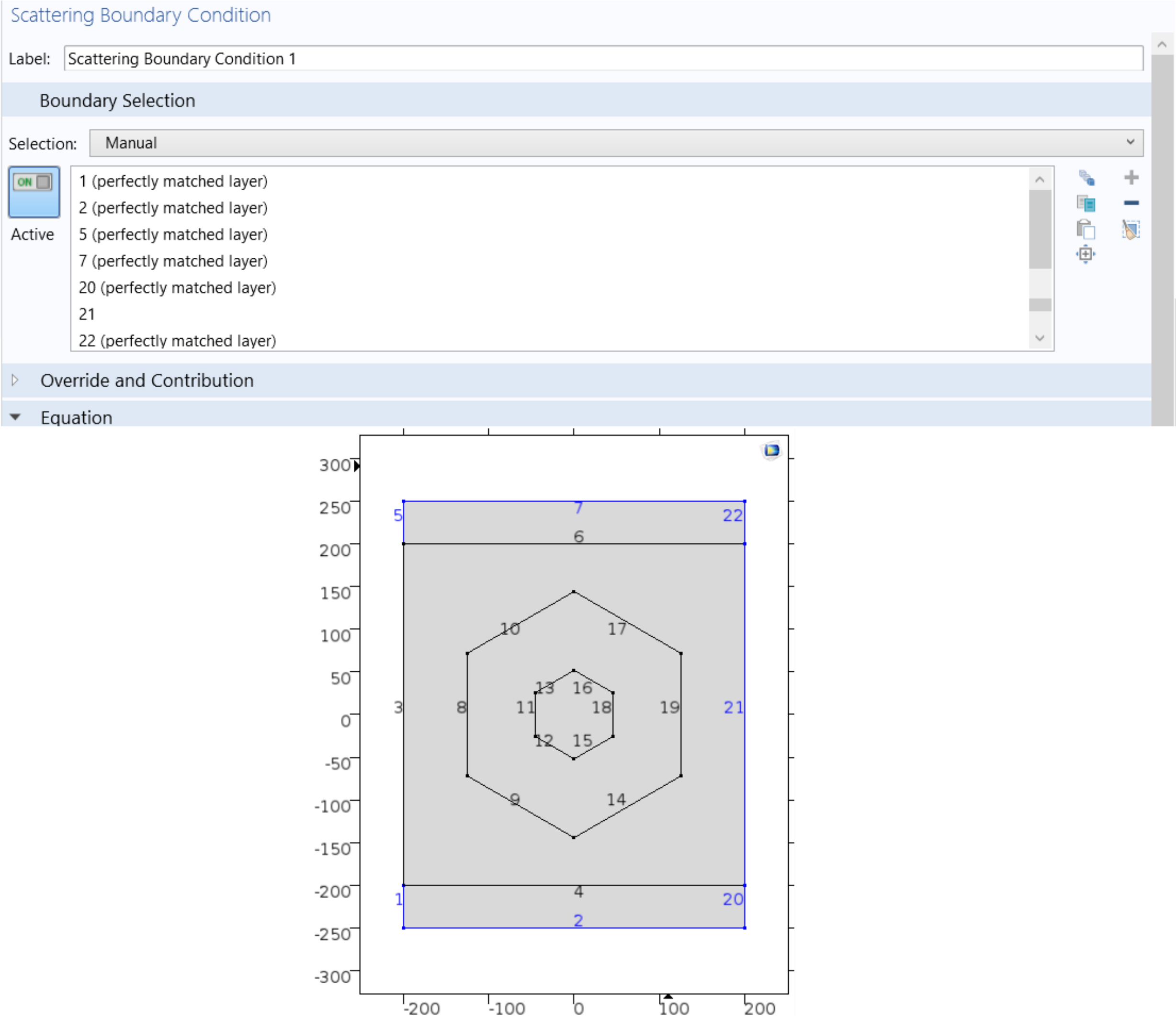

Scattering Boundary Condition

Label: Scattering Boundary Condition 1

Boundary Selection

Selection: Manual

- 1 (perfectly matched layer)
- 2 (perfectly matched layer)
- 5 (perfectly matched layer)
- 7 (perfectly matched layer)
- 20 (perfectly matched layer)
- 21
- 22 (perfectly matched layer)

2.4.2 Scattering Boundary Condition 2

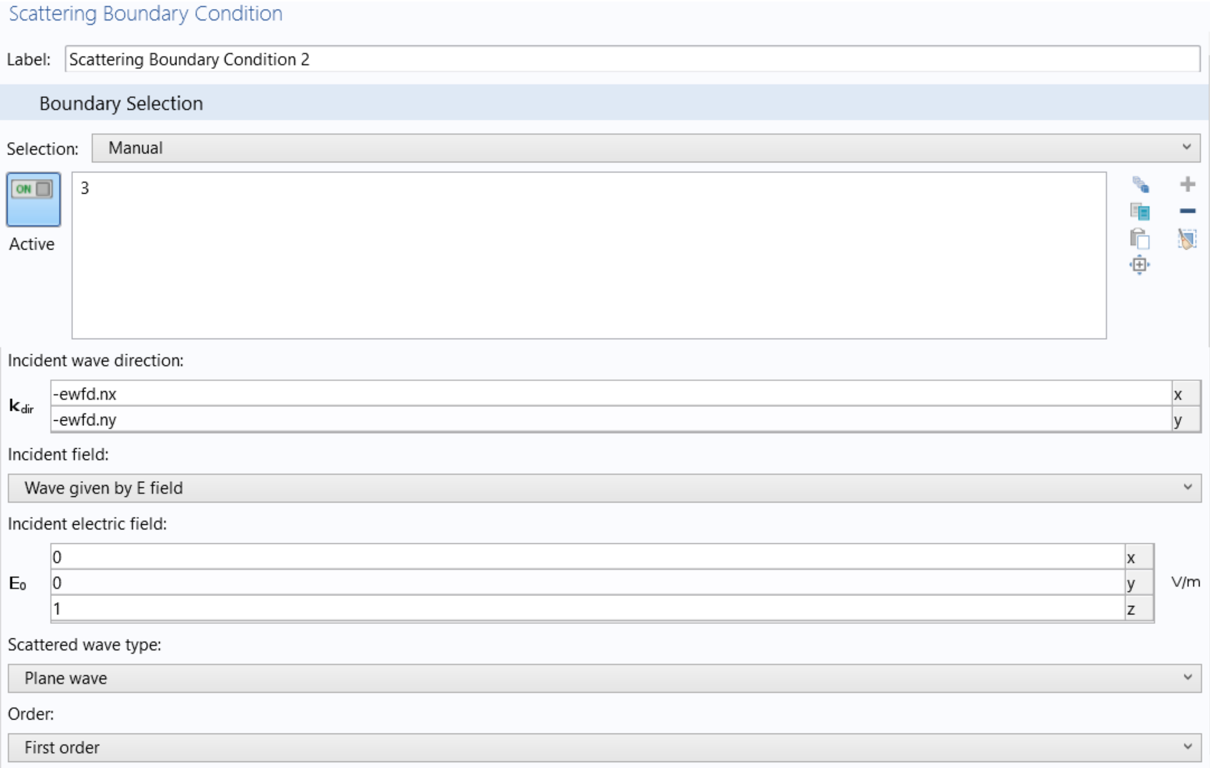

Scattering Boundary Condition

Label: Scattering Boundary Condition 2

Boundary Selection

Selection: Manual

3

Active

Incident wave direction:

k_{dir} x: -ewfd.nx

k_{dir} y: -ewfd.ny

Incident field: Wave given by E field

Incident electric field:

E_0 x: 0

E_0 y: 0

E_0 z: 1 V/m

Scattered wave type: Plane wave

Order: First order

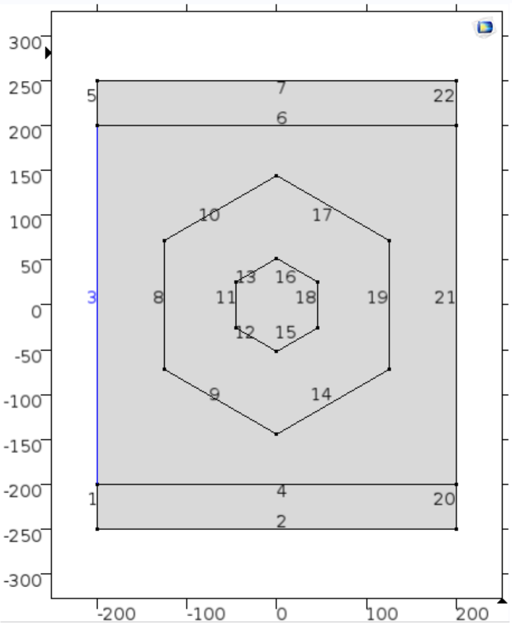

2.5 Mesh

The mesh size was initially chosen to be Fine while the model was being developed. However, the final simulation uses an Extra Fine mesh to provide a higher degree of accuracy for the calculations.

2.5.1 Size

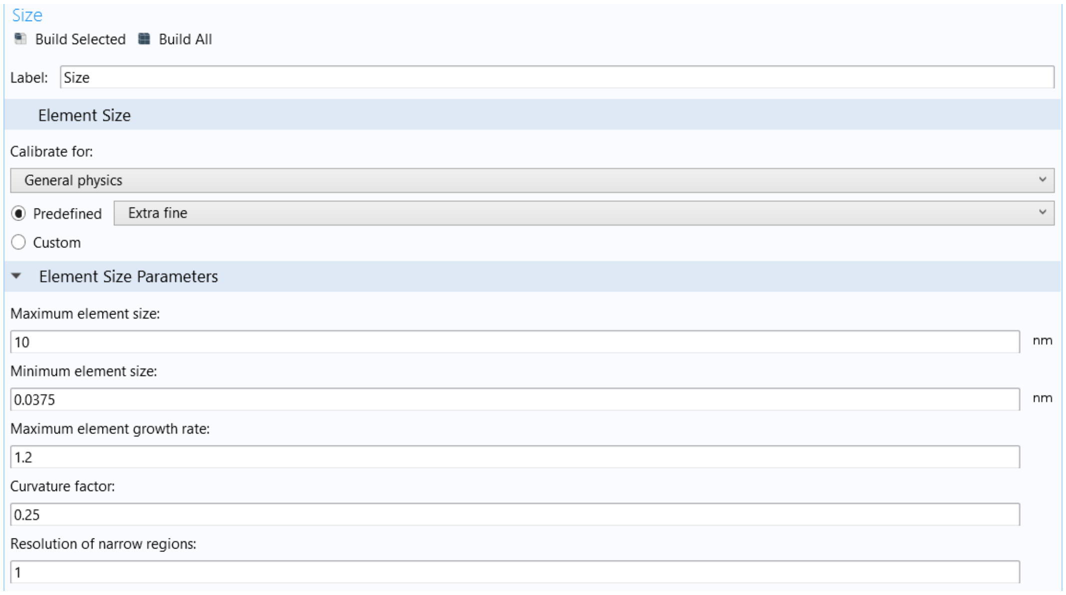

Label: Size

Calibrate for: General physics

● Predefined Extra fine

○ Custom

Maximum element size: 10 nm

Minimum element size: 0.0375 nm

Maximum element growth rate: 1.2

Curvature factor: 0.25

Resolution of narrow regions: 1

3. STUDY

3.1 Parametric Sweep

The simulation uses a parametric sweep over the MgO thicknesses from 2 to 80 nm in 2 nm increments. Each MgO thickness is simulated separately with the results accessible within the Results section.

Label: Parametric Sweep

Sweep type: Specified combinations

Parameter name	Parameter value list	Parameter unit
tM (MgO Thickness)	range(2,2,80)	

4. RESULTS

One of the advantages to using COMSOL instead of Lumerical to simulate systems is that COMSOL calculates and stores multiple data sets within a single simulation. After running a COMSOL simulation, it is possible to access the intensity maps of the electric field for each MgO thickness, perform line and surface integrations of any of the edges or areas within the model to compare and quantify the results, and export all of the graphical intensity maps as an animation that will sweep through the MgO thicknesses.

4.1 Derived Values

Line and surface integrals can be calculated within this section and the results stored within the Tables Section with the columns representing MgO thicknesses.

4.2 Tables

The tables generated by the line and surface integrals can be displayed within this section or exported as .csv files for use with Excel or other program.

4.3 Electric Field

The intensity maps of the electric field can be plotted and exported individually within this section.

4.4 Export

An animation that will cycle through all of the electric field intensity maps within the parameter space can be generated here. The available animation formats include gif and avi.

REFERENCES

1. Wu PH, Tsai PH, Wu ML, Chuang TC, Shih YY, Chung HW*, et al.* "High spatial resolution brain functional MRI using submillimeter balanced steady-state free precession acquisition". *Med Phys* 2013, **40**(12)**:** 122304.

2. Goldman LW. "Principles of CT: Multislice CT". *J Nucl Med Technol* 2008, **36**(2)**:** 57-68.

3. Vaquero JJ, Kinahan P. "Positron emission tomography: Current challenges and opportunities for technological advances in clinical and preclinical imaging systems". *Annu Rev Biomed Eng* 2015, **17:** 385-414.

4. Bar-Shalom R, Yefremov N, Guralnik L, Gaitini D, Frenkel A, Kuten A*, et al.* "Clinical performance of PET/CT in evaluation of cancer - additional value for diagnostic imaging and patient management". *The Journal of Nuclear Medicine* 2003, **44**(8)**:** 1200-1209.

5. Shreve PD. "Adding structure to function". *J Nucl Med* 2000, **41**(8)**:** 1380-1382.

6. Peller P, Subramaniam R, Guermazi A. *PET-CT and PET-MRI in Oncology - A Practical Guide*. Springer-Verlag Berlin Heidelberg: London, 2012.

7. Granov A, Tiutin L, Schwarz T. *Positron Emission Tomography*. Springer-Verlag Berlin Heidelberg: New York, 2013.

8. Hagge RJ, Wong TZ, Coleman RE. "Positron emission tomography - Brain tumors and lung cancer". *Radiologic Clinics of North America* 2001, **39**(5)**:** 871-881.

9. Binderup T, Knigge U, Loft A, Federspiel B, Kjaer A. "18F-fluorodeoxyglucose positron emission tomography predicts survival of patients with neuroendocrine tumors". *Clin Cancer Res* 2010, **16**(3)**:** 978-985.

10. Folpe AL, Lyles RH, Sprouse JT, Conrad III EU, Eary JF. "(F-18) Fluorodeoxyglucose positron emission tomography as a predictor of pathologic grade and other prognostic variables in bone and soft tissue sarcoma". *Clinical Cancer Research* 2000, **6:** 1279-1287.

11. Robbins RJ, Wan Q, Grewal RK, Reibke R, Gonen M, Strauss HW*, et al.* "Real-time prognosis for metastatic thyroid carcinoma based on 2-[18F]fluoro-2-deoxy-D-glucose-positron emission tomography scanning". *J Clin Endocrinol Metab* 2006, **91**(2)**:** 498-505.

12. Mac Manus MP. "Positron emission tomography is superior to computed tomography scanning for response-assessment after radical radiotherapy or chemoradiotherapy in patients with non-small-cell lung cancer". *Journal of Clinical Oncology* 2003, **21**(7)**:** 1285-1292.

13. Alavi JB, Alavi A, Chawluk J, Kushner M, Powe J, Hickey W*, et al.* "Positron emission tomography in patients with glioma - A predictor of prognosis". *Cancer* 1988, **62**(6)**:** 1074-1078.

14. Jerusalem G, Beguin Y, Fassotte MF, Najjar F, Paulus P, Rigo P*, et al.* "Whole-body positron emission tomography using 18-F-fluorodeoxyglucose for posttreatment evaluation in hodgkin's disease and non-hodgkin's lymphoma has higher diagnostic and prognostic value than classical computed tomography scan imaging". *Blood* 1999, **94**(2)**:** 429-433.

15. Gallamini A, Hutchings M, Rigacci L, Specht L, Merli F, Hansen M*, et al.* "Early interim 2-[18F]fluoro-2-deoxy-D-glucose positron emission tomography is prognostically superior to international prognostic score in advanced-stage Hodgkin's lymphoma: a report from a joint Italian-Danish study". *J Clin Oncol* 2007, **25**(24)**:** 3746-3752.

16. Witte OD, Lefranc F, Levivier M, Salmon I, Brotchi J, Goldman S. "FDG-PET as a prognostic factor in high-grade astrocytoma". *Journal of Neuro-Oncology* 2000, **49:** 157-163.

17. Nassalski A, Kapusta M, Batsch T, Wolski D, Mockel D, Enghardt W*, et al.* "Comparative study of scintillators for PET/CT detectors". *IEEE Transactions on Nuclear Science* 2007, **54**(1)**:** 3-10.

18. Kamal A. *Nuclear Physics*. Springer-Verlag Berlin Heidelberg: London, 2014.

19. Nelson G, Reilly D. Gamma-Ray Interactions with Matter. *Passive Nondestructive Analysis of Nuclear Materials*: Los Alamos National Laboratory, 1991, pp 27-42.

20. Bailey DL, Townsend DW, Valk PE, Maisey MN. *Positron Emission Tomography - Basic Sciences*. Springer-Verlag: London, 2005.

21. Pidol L, Kahn-Harari A, Viana B, Virey B, Ferrand B, Dorenbos P*, et al.* "High efficiency of lutecium silicate scintillators, Ce-doped LPS and LYSO crystals". *IEEE Transactions on Nuclear Science* 2004, **51**(3)**:** 886-890.

22. Ishii M, Kobayashi M. "Single crystals for radiation detectors". *Prog Crystal Growth and Characterization* 1992, **23:** 245-311.

23. Van Eijk CWE. "Inorganic-scintillator development". *Nucl Instrum Methods Phys Res A* 2001(460)**:** 1-14.

24. Yanagida T. "Study of rare-earth-doped scintillators". *Optical Materials* 2013, **35**(11)**:** 1987-1992.

25. Nikl M. "Scintillation detectors for x-rays". *Measurement Science and Technology* 2006, **17**(4)**:** R37-R54.

26. Lecoq P. "New approaches to improve timing resolution in scintillators". *IEEE Transactions on Nuclear Science* 2012, **59**(5)**:** 2313-2318.

27. Schuster F, Laumer B, Zamani RR, Magen C, Morante JR, Arbiol J*, et al.* "p-GaN n-ZnO heterojunction nanowires - Optoelectronic properties and the role of interface polarity". *ACS Nano* 2014, **8**(5)**:** 4376-4384.

28. Hendrickson JR, Vangala S, Nader N, Leedy K, Guo J, Cleary JW. "Plasmon resonance and perfect light absorption in subwavelength trench arrays etched in gallium-doped zinc oxide film". *Applied Physics Letters* 2015, **107**(19)**:** 191906.

29. Lu J, Shi Z, Wang Y, Lin Y, Zhu Q, Tian Z*, et al.* "Plasmon-enhanced electrically light-emitting from ZnO nanorod arrays/p-GaN heterostructure devices". *Sci Rep* 2016, **6:** 25645.

30. Chou Y, Chou B, Chiang C, Lai Y, Yang C, Li H*, et al.* "Ultrastrong mode confinement in ZnO surface plasmon nanolasers". *ACS Nano* 2015, **9**(4)**:** 3978-3983.

31. Zhang C, Marvinney CE, Xu HY, Liu WZ, Wang CL, Zhang LX*, et al.* "Enhanced waveguide-type ultraviolet electroluminescence from ZnO/MgZnO core/shell nanorod array light-emitting diodes via coupling with Ag nanoparticles localized surface plasmons". *Nanoscale* 2015, **7**(3)**:** 1073-1080.

32. Li J, Lin Y, Lu J, Xu C, Wang Y, Shi Z*, et al.* "Single mode ZnO whispering-gallery submicron cavity and graphene improved lasing performance". *ACS Nano* 2015, **9**(7)**:** 6794-6800.

33. Zhang Q, Liu W, Sun C, Zhang H, Pang W, Zhang D*, et al.* "On-chip surface modified nanostructured ZnO as functional pH sensors". *Nanotechnology* 2015, **26**(35)**:** 355202.

34. Wei A, Pan L, Huang W. "Recent progress in the ZnO nanostructure-based sensors". *Materials Science and Engineering: B* 2011, **176**(18)**:** 1409-1421.

35. Nour ES, Bondarevs A, Huss P, Sandberg M, Gong S, Willander M*, et al.* "Low-frequency self-powered footstep sensor based on ZnO nanowires on paper substrate". *Nanoscale Res Lett* 2016, **11**(1)**:** 156.

36. Klingshirn C. "ZnO: From basics towards applications". *physica status solidi (b)* 2007, **244**(9)**:** 3027-3073.

37. Özgür U, Alivov YI, Liu C, Teke A, Reshchikov MA, Doğan S*, et al.* "A comprehensive review of ZnO materials and devices". *Journal of Applied Physics* 2005, **98**(4)**:** 041301.

38. Simpson PJ, Tjossem R, Hunt AW, Lynn KG, Munné V. "Superfast timing performance from ZnO scintillators". *Nuclear Instruments and Methods in Physics Research Section A: Accelerators, Spectrometers, Detectors and Associated Equipment* 2003, **505**(1-2)**:** 82-84.

39. McCluskey MD, Jokela SJ. "Defects in ZnO". *Journal of Applied Physics* 2009, **106**(7)**:** 071101.

40. Park C, Lee J, Chang WS. "Geometrical separation of defect states in ZnO nanorods and their morphology-dependent correlation between photoluminescence and photoconductivity". *The Journal of Physical Chemistry C* 2015, **119**(29)**:** 16984-16990.

41. Empizo MJF, Yamanoi K, Fukuda K, Arita R, Minami Y, Shimizu T*, et al.* "Photoluminescence investigations of bulk and microstructured ZnO crystals for scintillator applications". *Journal of Ceramic Processing Research* 2015, **16**(1)**:** 98-101.

42. Al-Hamadi NA, Al-Alawy RD, Hassan SJ. "Effect of gamma irradiation on the structural and optical properties of ZnO thin films". *IOSR Journal of Computer Engineering* 2014, **16**(1)**:** 11-16.

43. Neal JS, DeVito DM, Armstrong BL, Hong M, Kesanli B, Yang X*, et al.* "Investigation of ZnO-based polycrystalline ceramic scintillators for use as alpha-particle detectors". *IEEE Transactions on Nuclear Science* 2009, **56**(3)**:** 892-898.

44. Zhao CX, Li YF, Chen YC, Wu JQ, Wang B, Yi FT*, et al.* "Microstructure change of ZnO nanowire induced by energetic x-ray radiation and its effect on the field emission properties". *Nanotechnology* 2013, **24**(27)**:** 275703.

45. Gorokhova EI, Anan'eva GV, Demidenko VA. "Optical, luminescence, and scintillation properties of ZnO and ZnO-Ga ceramics". *J Opt Technol* 2008, **75**(11)**:** 741-746.

46. Neal JS, Giles NC, Yang X, Wall RA, Ucer KB, Williams RT*, et al.* "Evaluation of melt-grown, ZnO single crystals for use as alpha-particle detectors". *IEEE Transactions on Nuclear Science* 2008, **55**(3)**:** 1397-1403.

47. Neal JS, Boatner LA, Giles NC, Halliburton LE, Derenzo SE, Bourret-Courchesne ED. "Comparative investigation of the performance of ZnO-based scintillators for use as α-particle detectors". *Nuclear Instruments and Methods in Physics Research Section A: Accelerators, Spectrometers, Detectors and Associated Equipment* 2006, **568**(2)**:** 803-809.

48. Derenzo SE, Bourret-Courshesne E, Bizarri G, Canning A. "Bright and ultra-fast scintillation from a semiconductor?". *Nucl Instrum Methods Phys Res A* 2016, **805:** 36-40.

49. Yanagida T, Fujimoto Y, Yamanoi K, Kano M, Wakamiya A, Kurosawa S*, et al.* "Optical and scintillation properties of bulk ZnO crystal". *physica status solidi (c)* 2012, **9**(12)**:** 2284-2287.

50. Kobayashi M, Komori J, Shimidzu K, Izaki M, Uesugi K, Takeuchi A*, et al.* "Development of vertically aligned ZnO-nanowires scintillators for high spatial resolution x-ray imaging". *Applied Physics Letters* 2015, **106**(8)**:** 081909.

51. Nakazato T, Shimizu T, Yamanoi K, Sakai K, Takeda K, Nishi R*, et al.* "Evaluation of soft x-ray laser with in situ imaging device of high spatial resolution ZnO scintillator". *Japanese Journal of Applied Physics* 2011, **50:** 122202.

52. Gorokhova EI, Anan'eva GV, Eron'ko SB, Oreschenko EA. "Structural, optical, and scintillation characteristics of ZnO ceramics". *J Opt Technol* 2011, **78**(11)**:** 753-760.

53. Empizo MJF, Yamanoi K, Mori K, Arita R, Iwano K, Takabatake M*, et al.* "Gamma-ray irradiation effects on the optical properties of bulk ZnO single crystals". *Applied Physics Express* 2015, **8**(6)**:** 061101.

54. Look DC, Reynolds DC, Hemsky JW, Jones RL, Sizelove JR. "Production and annealing of electron irradiation damage in ZnO". *Applied Physics Letters* 1999, **75**(6)**:** 811.

55. Lehmann W. "Edge emission of n-type conducting ZnO and CdS". *Solid-State Electronics* 1966, **9:** 1107-1110.

56. Chen SL, Chen WM, Buyanova IA. "Dynamics of donor bound excitons in ZnO". *Applied Physics Letters* 2013, **102**(12)**:** 121103.

57. Derenzo SE, Weber MJ, Bourret-Courchesne E, Klintenberg MK. "The quest for the ideal inorganic scintillator". *Nuclear Instruments and Methods in Physics Research Section A: Accelerators, Spectrometers, Detectors and Associated Equipment* 2003, **505**(1-2)**:** 111-117.

58. Weber MJ. "Scintillation: mechanisms and new crystals". *Nuclear Instruments and Methods in Physics Research Section A: Accelerators, Spectrometers, Detectors and Associated Equipment* 2004, **527**(1-2)**:** 9-14.

59. Weber MJ. "Inorganic scintillators: Today and tomorrow". *Journal of Luminescence* 2002(100)**:** 35-45.

60. Conti M, Eriksson L. "Physics of pure and non-pure positron emitters for PET: a review and a discussion". *EJNMMI Phys* 2016, **3**(1)**:** 8.

61. Huang B, Law M, Khong P. "Whole-body PET/CT scanning: Estimation of radiation dose and cancer risk". *Radiology*, **251**(1)**:** 166-174.

62. Saha GB. *Basics of PET imaging*. Springer: New York, USA, 2005.

63. Chernobyl - Assessment of radiological and health impacts: Organisation for Economic Co-operation and Development - Nuclear Energy Agency; 2002.

64. Achim P, Monfort M, Le Petit G, Gross P, Douysset G, Taffary T*, et al.* "Analysis of radionuclide releases from the Fukushima Dai-ichi Nuclear Power Plant accident Part II". *Pure and Applied Geophysics* 2012, **171**(3-5)**:** 645-667.

65. Fetter S, Frolov V, Miller M, Mozley R, Prilutsky O, Rodionov S*, et al.* "Detecting nuclear warheads". *Science and Global Security* 1990, **1:** 225-302.

66. Yang S, Wang L, Wang Y, Li L, Wang T, Jiang Z. "Identification and characteristics of ZnO/MgO core-shell nanowires". *AIP Advances* 2015, **5**(3)**:** 037122.

67. Kuang W-J, Li Q, Sun Y, Chen J, Tolner H. "Near-band-edge emission characteristics of ZnO-MgO core-shell quantum-dots". *Materials Letters* 2016, **178:** 27-30.

68. Shi ZF, Zhang YT, Cui XJ, Zhuang SW, Wu B, Chu XW*, et al.* "Photoluminescence performance enhancement of ZnO/MgO heterostructured nanowires and their applications in ultraviolet laser diodes". *Phys Chem Chem Phys* 2015, **17**(21)**:** 13813-13820.

69. Grinblat G, Bern F, Barzola-Quiquia J, Tirado M, Comedi D, Esquinazi P. "Luminescence and electrical properties of single ZnO/MgO core/shell nanowires". *Applied Physics Letters* 2014, **104**(10)**:** 103113.

70. Wu Y, Wu W, Zou XM, Xu L, Li JC. "Growth and great UV emission improvement of highly crystalline quality core–shell ZnO/MgO nanowires". *Materials Letters* 2012, **84:** 147-150.

71. Song J-G, Park J, Yoon J, Woo H, Ko K, Lee T*, et al.* "Plasma enhanced atomic layer deposition of magnesium oxide as a passivation layer for enhanced

photoluminescence of ZnO nanowires". *Journal of Luminescence* 2014, **145:** 307-311.

72. Dong H, Sun S, Sun L, Zhou W, Zhou L, Shen X*, et al.* "Thermodynamic-effect-induced growth, optical modulation and UV lasing of hierarchical ZnO Fabry–Pérot resonators". *Journal of Materials Chemistry* 2012, **22**(7)**:** 3069.

73. Dong H, Liu Y, Sun S, Li J, Zhan J, Chen Z*, et al.* "Geometry dependent evolution of the resonant mode in ZnO elongated hexagonal microcavity". *Sci Rep* 2016, **6:** 19273.

74. Jin C, Kim H, Lee C. "Ultraintense short-wavelength emission from ZnO-sheathed MgO nanorods induced by subwavelength optical resonance cavity formation: Verification of previous hypothesis". *ACS Appl Mater Interfaces* 2012, **4**(3)**:** 1262-1266.

75. Zhang X, Zhang X, Xu J, Shan X, Xu J, Yu D. "Whispering gallery modes in single triangular ZnO nanorods". *Optics Letters* 2009, **34**(16)**:** 2533-2535.

76. Wang B, Jin X, Wu H, Zheng Z, Ouyang Z. "3D resonator based on luminescence enhanced by both polarized, size-dependent whispering gallery modes and Fabry-Perot waveguide modes in individual ZnO micro- and nanonails". *Nanoscale* 2014, **6**(10)**:** 5338-5342.

77. Wang B, Jin X, Wu HY, Zheng ZQ. "Whispering gallery and Fabry–Pérot modes enhanced luminescence from individual ZnO micro mushroom". *Journal of Applied Physics* 2013, **113**(3)**:** 034313.

78. Xu C, Dai J, Zhu G, Zhu G, Lin Y, Li J*, et al.* "Whispering-gallery mode lasing in ZnO microcavities". *Laser & Photonics Reviews* 2014, **8**(4)**:** 469-494.

79. Zhu GY, Li JT, Tian ZS, Dai J, Wang YY, Li PL*, et al.* "Electro-pumped whispering gallery mode ZnO microlaser array". *Applied Physics Letters* 2015, **106**(2)**:** 021111.

80. Dong HM, Yang YH, Yang GW. "Super low threshold plasmonic WGM lasing from an individual ZnO hexagonal microrod on an Au substrate for plasmon lasers". *Sci Rep* 2015, **5:** 8776.

81. Ni PN, Shan CX, Wang SP, Lu YJ, Li BH, Shen DZ. "Fabry-Pérot resonance enhanced electrically pumped random lasing from ZnO films". *Applied Physics Letters* 2015, **107**(23)**:** 231108.

82. Kirschbrown JR, House RL, Mehl BP, Parker JK, Papanikolas JM. "Hybrid standing wave and whispering gallery modes in needle-shaped ZnO rods: Simulation of emission microscopy images using finite difference frequency domain methods with a focused Gaussian source". *The Journal of Physical Chemistry C* 2013, **117**(20)**:** 10653-10660.

83. Jin C, Kim H, Ryu H-Y, Kim HW, Lee C. "Subwavelength optical resonant cavity-induced enhancement of the near-band-edge emission from ZnO-core/SnO2-shell nanorods". *The Journal of Physical Chemistry C* 2011, **115**(17)**:** 8513-8518.

84. Jiang Q, Zheng H, Wang J, Long H, Fang G. "Structural and optical characterization of ZnO/Mg(x)Zn(1-x)O multiple quantum wells based random laser diodes". *ACS Appl Mater Interfaces* 2012, **4**(12)**:** 7043-7046.

85. Xue M, Guo Q, Wu K, Guo J. "Initial oxidation and interfacial diffusion of Zn on faceted MgO(111) films". *Langmuir* 2008, **24**(16)**:** 8760-8764.

86. Johnson JC, Yan H, Yang P, Saykally RJ. "Optical cavity effects in ZnO nanowire lasers and waveguides". *J Phys Chem B* 2003, **107:** 8816-8828.

87. Chen B, Meng C, Yang Z, Li W, Lin S, Gu T*, et al.* "Graphene coated ZnO nanowire optical waveguides". *Opt Express* 2014, **22**(20)**:** 24276-24285.

88. Kim T-U, Gang M-G, Kim J-A, Moon J-H, Kim D-G, Kim S-H*, et al.* "The study of light waveguide effects on ZnO nanorod arrays". *Electronic Materials Letters* 2016, **12**(2)**:** 224-231.

89. Jiang DY, Zhao JX, Zhao M, Liang QC, Gao S, Qin JM*, et al.* "Optical waveguide based on ZnO nanowires prepared by a thermal evaporation process". *Journal of Alloys and Compounds* 2012, **532:** 31-33.

90. Hauschild R, Kalt H. "Guided modes in ZnO nanorods". *Applied Physics Letters* 2006, **89**(12)**:** 123107.

91. Voss T, Svacha GT, Mazur E, Muller S, Ronning C, Konjhodzic D*, et al.* "High-order waveguide modes in ZnO nanowires". *Nano Letters* 2007, **7**(12)**:** 3675-3680.

92. Johnson JC, Yan H, Choi HJ, Knutsen KP, Peterson PB, Law M*, et al.* Single nanowire waveguides and lasers. Physical Chemistry of Interfaces and Nanomaterials II; 2003; Bellingham, WA; 2003. p. 187-196.

93. Henneghien AL, Gayral B, Desieres Y, Gerard JM. "Simulation of waveguiding and emitting properties of semiconductor nanowires with hexagonal or circular sections". *J Opt Soc Am B* 2009, **26**(12)**:** 2396-2403.

94. Li C, Gao M, Zhang X, Peng L-M, Chen Q. "Spatially and angularly resolved cathodoluminescence study of single ZnO nanorods". *Journal of Nanoscience and Nanotechnology* 2010, **10**(11)**:** 7158-7161.

95. Urbieta A, del Campo R, Pérez R, Fernández P, Piqueras J. "Luminescence and waveguiding behavior in Tb doped ZnO micro and nanostructures". *Journal of Alloys and Compounds* 2014, **610:** 416-421.

96. Kar A, Ahern R, Gopalsami N, Raptis AC, Stroscio MA, Dutta M. "Preliminary investigation on the modification of electronic properties in surface passivated SnO2 nanowires with Schottky contacts on being exposed to 137Cs γ-radiation". *Journal of Applied Physics* 2012, **111**(8)**:** 084319.

97. Kaur A, Chauhan RP. "Effect of gamma irradiation on electrical and structural properties of Zn nanowires". *Radiation Physics and Chemistry* 2014, **100:** 59-64.

98. Rana P, Chauhan RP. "Size and irradiation effects on the structural and electrical properties of copper nanowires". *Physica B: Condensed Matter* 2014, **451:** 26-33.

99. Gehlawat D, Chauhan RP. "Study of electronic transport in gamma ray exposed nanowires". *Materials Research Bulletin* 2014, **49:** 454-461.

100. Li Y, Dong X, Gao J, Hei D, Zhou X, Zhang H. "A highly sensitive γ-radiation dosimeter based on the CeO2 nanowires". *Physica E: Low-dimensional Systems and Nanostructures* 2009, **41**(8)**:** 1550-1553.

101. Locker DR, Meese JM. "Displacement thresholds in ZnO". *IEEE Transactions on Nuclear Science* 1972, **4**(18)**:** 237-242.

102. Fink K. "Ab initio cluster calculations for the absorption energies of F and F+ centers in bulk ZnO". *Phys Chem Chem Phys* 2005, **7**(16)**:** 2999-3004.

103. D'Amico NR, Cantele G, Ninno D. "First-principles calculations of clean and defected ZnO surfaces". *The Journal of Physical Chemistry C* 2012, **116**(40)**:** 21391-21400.

104. Soriano V, Galland D. "Photosensitivity of the EPR spectrum of the F+ center in ZnO". *physica status solidi (b)* 1976, **77:** 739-743.

105. Kavanoz HB, Yağci Ö, Yalçın Z, İçelli O, Altındal A, Okutan M*, et al.* "Photon parameters for γ-rays sensing properties of some thick oxide films". *Vacuum* 2014, **101:** 238-245.

106. Wang X, Song J, Li P, Ryou JH, Dupuis RD, Summers CJ*, et al.* "Growth of uniformly aligned ZnO nanowire heterojunction arrays on GaN, AIN, and AlGaN substrates". *J Am Chem Soc* 2005, **127**(21)**:** 7920-7923.

107. Xu S, Wang ZL. "One-dimensional ZnO nanostructures: Solution growth and functional properties". *Nano Research* 2011, **4**(11)**:** 1013-1098.